On the equilibration of asymmetric barotropic instability *

Nili Harnik

Department of Geophysical, Atmospheric and Planetary Sciences,

Tel–Aviv University, Tel Aviv, 69978, Israel

David G. Dritschel

School of Mathematics and Statistics,

University of St Andrews, St Andrews, KY16 9SS, Scotland

Eyal Heifetz

Department of Geophysical, Atmospheric and Planetary Sciences,

Tel–Aviv University, Tel Aviv, 69978, Israel

and Department of Meteorology, Stockholm University.

November 28, 2013

*Corresponding author address: Nili Harnik, Department of Geophysics and Planetary Sciences, Tel–Aviv University, Israel. Email: harnik@tau.ac.il

Abstract

The conjunction of turbulence, waves and zonal jets in geophysical flows gives rise to the formation of potential vorticity staircases and to the sharpening of jets by eddies. The effect of eddies on jet structure, however, is fundamentally different if the eddies arise from barotropic rather than from baroclinic instability. As is well known, barotropic instability may occur on zonal jets when there is a reversal of potential vorticity gradients at the jet flanks. In this paper we focus on the nonlinear stages of this instability and its eventual saturation. We consider an idealized initial state consisting of an anti-cyclonic potential vorticity strip sitting in the flanks of an eastward jet. This asymmetric configuration, a generalization of the Rayleigh problem, is one of the simplest barotropic jet configurations which incorporates many fundamental aspects of real flows, including linear instability and its equilibration, nonlinear interactions, scale cascades, vortex dynamics, and jet sharpening. We make use of the simplicity of the problem to conduct an extensive parameter sweep, and develop a theory relating the properties of the equilibrated flow to the initial flow state by considering the marginal stability limit, together with conservation of circulation and wave activity.

1 Introduction

Complex interrelations between turbulence, waves and zonal jets shape the flow in the atmosphere, the oceans and in other planetary atmospheres. Turbulent motions horizontally mix potential vorticity (PV), and when wave motions exist, such as Rossby waves on a meridional gradient of the background PV, they organize the fluid motions at the wave scale, limiting the upscale cascade of energy occurring in homogeneous turbulence (e.g Rhines, 1975). An inherent feature of rotating turbulent flows is the spontaneous emergence of jets (Rhines, 1975; McIntyre, 1994). For Rossby waves, the meridional momentum flux is directed opposite to the direction of meridional wave activity propagation (Eliassen and Palm, 1961). Thus, waves which are generated at a certain latitude will flux momentum into that region when they propagate away, inducing a jet at that latitude. At the same time, when eddies are forced in the presence of a preexisting barotropic jet (e.g. by small-scale turbulence), the shearing of the eddies by the mean flow tilts the eddies with the shear, resulting in a momentum flux convergence pattern which tends to sharpen the jet (e.g. Dritschel and Scott, 2010). This leads to a positive feedback and allows jets to dominate the statistically equilibrated state. At the jet flanks, the eddies tend to mix PV, leading to the formation of a PV staircase – regions of approximately constant PV, separated by sharp gradients at which the jets are located (Dritschel and McIntyre, 2008; Scott and Dritschel, 2012).

During this process of the jet enhancement, the eddies get sheared by the flow, leading to a decrease in eddy kinetic energy. Thus, to maintain a statistically steady state, the eddies need to be forced. Common eddy forcing mechanisms discussed in the literature are baroclinic instability in the Earth's atmosphere (e.g. Panetta, 1993) and deep convection in Jupiter (Rogers, 1995; Ingersoll et al, 2004). While baroclinic instability is the main source of atmospheric disturbances, there is some evidence that barotropic instability also plays an important role, for example, in

ITCZ breakdown (Ferreira and Schubert, 1997), in mixing within critical layers (Haynes, 1985, 1989), and as suggested more recently, in compensating for the localized forcing of the zonal flow by gravity waves in the stratosphere (Cohen et al, 2013). Moreover, it is also possible that during the flow evolution, weak forcing may cause negative meridional gradients of PV to form at the jet flanks, allowing for barotropic instability to develop between the jet center and its flanks. Since barotropically unstable growing waves are tilted against the meridional shear, they alone act to weaken and broaden the jet, rather than sharpen it.

In the present work, we specifically examine an unforced, barotropically unstable flow, studying in detail how instability affects the evolution of jets and determines their final equilibrated form. To this end, we examine the evolution of a uniform anti-cyclonic PV strip adjacent to a PV staircase on a barotropic β-plane (shown in figure 1a). This is a modified Rayleigh-Kuo problem (Rayleigh, 1880; Kuo, 1949), in which the positive PV jump is divided into two steps, and the sum of these two positive jumps is larger than the negative jump. The negative (anti-cyclonic) PV anomaly subsequently breaks up into a street of negative vortices, but unlike the symmetric Rayleigh problem (in which the positive and negative PV jumps are of the same magnitude), a positive PV jump remains, on which waves evolve. As we will show, this highly simplified problem is nevertheless very rich, and allows us to study the fundamental and complex interrelation between the mean flow, Rossby waves and vortices. Moreover, separating the positive PV jump into two steps allows us to also examine the process of jet sharpening.

The choice of a piecewise-constant PV mean flow structure is motivated primarily by the resulting simplicity of the problem, but also by the observation that PV staircases can emerge on rotating planets in realistic parameter regimes (see Scott and Dritschel, 2012 & references therein). Moreover, PV gradients are often concentrated in narrow zones in the real atmosphere (e.g. Hoskins et al, 1985) and evidently in the atmospheres of the gas giant planets (c.f.

Marcus, 1993). The simple PV structure adopted allows a full specification of the mean flow profile with only 4 independent parameters, one of which is the domain-averaged meridional shear. By assuming this parameter is zero (leaving an examination of its effect for a later study), we are left with only three independent external parameters: the gap between the positive PV jumps, the amplitude of the negative PV strip, and the planetary vorticity gradient. These parameters nonetheless allow for a rich variety of unstable initial mean flows, permitting us to examine how flow equilibration and jet sharpening depend on the external parameters, and furthermore how waves and turbulence evolve and interact with each other and the mean flow. As such, this study extends Nielsen and Schoeberl's (1984) study of the nonlinear equilibration of a barotropic point jet, and complements Dritschel and Scott (2010) which examined the sharpening of an initially broad and stable barotropic jet by externally imposed turbulence.

The paper is structured as follows. After detailing the problem set up in section 2, we show results from a typical control run in section 3, first describing the key stages in the flow evolution (3.1) and examining jet sharpening (3.2). Then in section 4 we examine the role of linear instability and, in particular, the relevance of quasi-linear dynamics to the temporal evolution of the flow. We then describe results from the full parameter sweep (section 5) and from this propose a simple model of the dependence of the flow evolution and its equilibration on the initial flow. A few conclusions are offered in section 6, followed by details of the numerical method, special equations and linear stability in the appendices.

2 Problem formulation

We employ the single-layer quasi-geostrophic (QG) equations,

$$\frac{\mathrm{D}q}{\mathrm{D}t} = \frac{\partial q}{\partial t} + \boldsymbol{u} \cdot \boldsymbol{\nabla} q = 0 \tag{1}$$

$$\nabla^2 \psi = q - \beta y \tag{2}$$

$$u = -\frac{\partial \psi}{\partial y} \qquad v = \frac{\partial \psi}{\partial x} \tag{3}$$

consisting of a single dynamical equation expressing material conservation of potential vorticity (PV) q and linear inversion relations providing the velocity field (u, v) in terms of q, here for the simplest case of an infinite radius of deformation in which the PV q reduces to the absolute vorticity. $q - \beta y$ is the corresponding relative vorticity or vorticity anomaly (β is the constant planetary vorticity gradient) and ψ is the streamfunction, The domain is a periodic channel, without loss of generality of length 2π in x (periodic), and of width L_y in y (with free-slip boundaries at $y = 0$ and L_y).

Our aim is to determine how nonlinear energy and enstrophy cascades and jet sharpening processes take place as an initially unstable flow equilibrates. For maximal simplicity, we consider a zonal jet consisting of just two equal 'poleward' jumps in PV, without loss of generality of magnitude $\Delta q_0 = 2\pi$, shown in figure 1a. The jumps are separated by a gap g in y. Alone, these jumps induce a blunt jet (two overlapping jets, with nearly uniform flow speeds in the narrow gap). Reducing g to zero intensifies the jet. In this way, we can study jet sharpening by the reduction of the distance between the two jumps, which when disturbed, may become complicated curves or contours (see below). Alone, these jumps comprise a monotonic PV distribution, and hence are stable, even to nonlinear disturbances (Dritschel, 1988a). To induce jet sharpening, we add a third, opposite-signed PV jump at a distance w below the two jumps already introduced. Taking q_1 to be the PV below the opposite-signed PV jump (in $y \in [0, y_1]$), we set the PV above this jump (in $y \in [y_1, y_2]$ where $y_2 = y_1 + w$) to be $q_2 = q_1 - \gamma\Delta q_0$. Between the original two jumps (in $y \in [y_2, y_3]$ where $y_3 = y_2 + g$), we set the PV to $q_3 = q_1 + \Delta q_0$. Then, the PV above the uppermost jump (in $y \in [y_3, L_y]$) is $q_4 = q_1 + 2\Delta q_0$. To centre the configuration, we choose $(y_1 + y_3)/2$ to lie at the domain centre, $L_y/2$; then $y_1 = (L_y - g - w)/2$, $y_2 = (L_y - g + w)/2$ and $y_3 = (L_y + g + w)/2$.

The value of q_1 is chosen to ensure that there is no net shear across the domain: $u(0) = u(L_y)$. This requires $\int_0^{L_y} (q - \beta y) dy = 0$, leading to $q_1 = \beta L_y/2 + \Delta q_0[(\gamma + 1)w/L_y - 1]$. A mean shear may be easily incorporated, but this is left for a future study. The values of $u(0) = u(L_y)$ are set by the additional requirement that the average zonal velocity vanishes, $\int_0^{L_y} u dy = 0$, though this choice is not important for the dynamical evolution of the flow (it merely translates the reference frame). The undisturbed PV distribution is illustrated in figure 1a. The domain aspect ratio L_x/L_y and numerical resolution (see below) were chosen to ensure adequate resolution of the lengths g and w and of the mature stages of the instability, which exhibits a growth in scale along the jet (an inverse energy cascade). After much experimentation, which included performing runs at half and quarter resolutions to check sensitivity, we decided to fix the width w of the anti-cyclonic zone below the double jump at $w = L_y/40$ in a domain of width $L_y = \pi/2$ (hence $L_x/L_y = 4$). Then, the key physical parameters are (see figure 1a):

- $\alpha = g/w$: the dimensionless width of the gap between the two positive PV jumps,
- γ: the ratio of the anti-cyclonic shear to Δq_0, and
- $\hat{\beta} = \beta w/\Delta q_0$: the variation of the PV across the anti-cyclonic zone, divided by Δq_0.

All runs are carried out to $t = 50$, corresponding to 50 characteristic 'eddy-turnaround' times, based on the PV contrast (4π) across the double jump.

To help understand how the nonlinear equilibration and jet sharpening depend on these parameters, we chose $\alpha \in \{0, 0.5, 1, 2\}$, $\gamma \in \{0.5, 1, 2\}$, and $\hat{\beta} \in \{0, 0.05, 0.1, 0.15, 0.2\}$, giving a total of 60 cases.

We use the Combined Lagrangian Advection Method (CLAM, Dritschel and Fontane (2010)) for our numerical simulations. This highly-accurate hybrid method, based on contour advection (Dritschel and Ambaum, 1997) and standard pseudo-spectral techniques, allows for very high numerical accuracy at low computational cost, permitting us to carry out a wide parameter sweep. Details of the numerical method are given in appendix A.

3 The control run

3.1 Evolution stages

We start by describing the main, typical characteristics of the flow evolution, using a control run. The general features of the flow evolution are similar in many respects to other existing studies of the equilibration of a barotropically unstable jet (e.g. Schoeberl and Lindzen, 1984; Nielsen and Schoeberl, 1984; Dritschel 1989; and Vallis, 2006, figure 6.6), but our focus is different. Moreover, our numerical simulations are carried out at substantially higher resolutions than in previous studies permitting us to see new, evidently generic features not evident in lower resolution simulations. We will emphasis the features of the evolution which are important for our discussion.

We choose a control run for which the gap width is equal to the width of the negative PV strip ($\alpha = 1$), the negative PV jump is equal to each of the positive jumps ($\gamma = 1$), and $\hat{\beta} = 0.05$ — not zero, but small enough to have a westerly jet as in observations (at large $\hat{\beta}$ we get strong easterly jets at the flanks of the domain). The initial and final zonal mean zonal wind and PV profiles for these parameters are shown in figure 2. We see a single eastward jet, flanked by westward flow. Initially, there are sharp meridional changes in the zonal mean wind shear, corresponding to the initial meridional PV jumps. This initial profile is unstable, and as we will show in Fig. 3, barotropic Rossby waves develop, mixing the negative PV strip mostly southwards into the adjacent PV region until it almost disappears. The final PV profile is monotonically increasing in the region initially occupied by PV jumps. Furthermore, the jet becomes weaker, smoother, and slightly broader (see dashed lines in figure 2).

Figure 3 shows instantaneous longitude-latitude sections of the PV field (shading), chosen during different stages of the evolution. At time $t = 2$, the initial PV structure is still evident, with the low PV strip (q_2) in darkest gray, and the gap region (q_3) rendered by the second lightest gray shading, just north of q_2. The waves evident on the interface have a zonal wavenumber of the most unstable normal mode (see section 4). At later times, these waves roll-up and break into vortices ($t = 4$). This nonlinear roll up is similar to that found in the Rayleigh problem (e.g. Dritschel, 1989; Vallis, 2006, figure 6.6). As time advances, the vortices shear and pair, while the dominant wavenumber of the interface undulations decreases ($t = 10$). During this process, low PV material from the vortices gets mixed into the southernmost PV region, and some gap material gets ejected into thin filaments within adjacent regions. As the anti-cyclonic vortices get smaller, the interface waves grow both in amplitude and wavelength, and dominate the flow field so that the vortices circle around within the larger interface wave regions. This is seen at $t = 16$ where the flow in one section is indicated by white arrows. The vortex pairing and growth of the interface wavelength halt when the vortices mix into their surrounding, leaving two relatively homogenized PV regions with a gap region in between, which is almost completely eliminated in some regions and only slightly narrowed in others ($t = 46$). We will show later that the total amount of fluid in the gap region has reduced significantly from the initial to the final stages. We see that the smooth meridional gradient of zonal mean PV in the final state (figure 2b) is an artifact of the averaging of the wavy PV staircase structure. Sharp PV gradients persist at all times.

The growth of wave amplitude is clearly evident in the domain-integrated eddy kinetic energy (EKE) and enstrophy, both plotted in figure 4a. As in Nielsen and Schoeberl (1984), we find down-gradient PV fluxes which spread meridionally during the nonlinear eddy growth stage and then oscillate during the saturated stage. This indicates that such flow evolution features may be common to many flow configurations.

We next examine the spectral evolution of the flow. From the eddy energy spectrum $E_k(y,t)$ (the portion of EKE in (zonal) wavenumber k, with the subscript k denoting the k^{th} component of the Fourier transform), we define a characteristic wavenumber as follows:

$$k_e(t) \equiv \frac{\int_0^{L_y} \sum_{k=1}^{n_x/2} k E_k(y,t) dy}{\int_0^{L_y} \sum_{k=1}^{n_x/2} E_k(y,t) dy} \tag{4}$$

where here $n_x = 1024$. This wavenumber essentially picks out the number of interface undulations. Figure 4b shows its evolution, plotted over the EKE spectrum. We see that k_e represents the peak EKE wavenumber well. The wavenumber is largest between $t = 2$ and 3, when the linear instability saturates. In the next section we show that k_e is the (linearly) most unstable wavenumber of the initial mean flow configuration. Note that we initialize the flow with a perturbation having a wavelength much larger than the most unstable mode, and thus it takes time for the most unstable mode to emerge. After the initial growth stage, k_e starts decreasing, signifying an upscale energy cascade. This cascade is fastest during the stage when EKE and eddy enstrophy grow. Thus, the eddies initially grow by linear instability and then by a (nonlinear) upscale energy cascade. During the upscale cascade stage, the negative zonal mean PV region spreads southwards and widens. As shown below, the robust positive meridional eddy PV flux can be explained by the southward moving or spreading of the anti-cyclonic vortices (a negative meridional drift of negative PV).

The upscale energy cascade continues until around $t = 15$, after which we see relatively constant eddy amplitudes and wavenumbers (figures 4a,b). The mean flow also stabilizes, with the meridional PV gradient region remaining constant in width. The remaining weak anti-cyclonic vortices now circle around within large wave crests, so that the southern edge of the mixed PV region also assumes a wavy shape (e.g. $t = 16$, figure 3). During this stage, the PV fluxes become much smaller and are more variable (they are not downgradient any more, not shown). This suggests that the interface now mostly evolves on its own, and is no longer significantly influenced by the much diminished vortices.

Two-dimensional homogeneous QG turbulence is characterized by a downscale enstrophy cascade, alongside an upscale energy cascade (Fjørtoft, 1953). Figure 5 shows an enstrophy-based wavenumber k_{ens}, similar to k_e (as in Eq. 4, but with eddy enstrophy instead of EKE), calculated for two regions, one near the PV interface ($0.7 \leq y \leq 0.9$) and one at $0.3 \leq y \leq 0.6$, where the vortices shear and merge (after they reach the region at around t=10). We see that in the region of vortex shearing and pairing, the behavior is turbulent with enstrophy cascading to smaller scales (thin line after $t = 15$), while in the interface region the enstrophy cascades to larger scales, like the EKE. The coherent interface structure traps enstrophy, enabling it in this region to cascade to large scales like energy. Similarly, in homogeneous QG turbulence, coherent vortices trap a portion of the enstrophy, enabling it to cascade to larger scales by vortex pairing (Dritschel et al, 2009). This is not inconsistent with the net direct, downscale cascade of enstrophy.

3.2 Jet sharpening

One of the goals of this study is to understand jet sharpening, which in this case is manifest as a narrowing of the gap region. From figure 3 (showing snapshots of the PV field) it is clear that gap material is ejected when the negative PV strip breaks up into vortices, and when vortices shear and pair during the nonlinear upscale cascade stage. The processes which extrude gap material are highly localized, so that after a while the gap width becomes variable in the horizontal direction. This is seen most clearly during the saturation stage, when "dragon-head" filamentary structures form on the interface (figure 6). These exquisitely complex fine-scale structures, which form by a localized sequence of filamentations of the PV interface (c.f. Dritschel, 1988b), capture most of the gap material inside them, so that upstream of the dragon-head the jump is exceedingly sharp. These structures are found in all the runs, across the parameter space, and appear to be a ubiquitous nonlinear feature of barotropic jet instability. To our knowledge, these dragon-head structures have never been seen before due to lack of numerical resolution.

We next look more closely at jet sharpening by examining the evolution of the gap between the two positive PV jumps. To quantify the gap evolution we find the PV contours which wrap the domain and bound the gap from both sides (making use of the built-in PV contour tracking routine in our numerical scheme) and determine how much material lies between them for a given longitudinal section. This is done by calculating the mean distance between the two contours, which in some locations have a complex filamentary structure (shown by the thin black lines in figure 6). Figure 7a shows a probability distribution function of the different gap width values, at the final time of the control run. Consistent with the bunching up of all gap material within dragon-head features, we see an essentially bi-modal distribution. Nearly half of the gap has narrowed by more than 80% (the peak at around 0.2), and another section has narrowed by about 30% (peak between 0.6-0.8). Note, however that in some sectors (which constitute about 14% of the longitude range), the gap has actually widened, in some cases by more than 50% (as evidenced by non-zero probability distribution function values beyond 1.5).

Figure 7b shows the time evolution of the zonal mean width of the gap, and the mean width of the narrowest 25% of the gap. Since the gap width calculation is numerically intensive, we only perform it every 5 time units. The gap narrows most rapidly during the vortex shearing and pairing stage (from $t = 0$ to 10) with the narrowest regions reaching a width of less than 10% of the initial width, and the mean gap reaching 60% of it. After the vortex shearing stage, the width of the narrowest gap regions oscillates slowly between 10 and 30%. In summary, our results demonstrate that jet sharpening — the result of nonlinear wave breaking — does not occur everywhere along the jet, but instead is highly inhomogeneous.

4 The role of quasi-linear dynamics

The evolution stages described above suggest there are two growth stages: a short initial linear growth stage, and a longer subsequent nonlinear growth stage. To examine the differences between these evolution stages more quantitatively, we perform a linear stability analysis for the zonal mean fields, for each model output time. Figure 8a shows the linear growth rate as a function of wavenumber and time (in shading) for the control run, along with the time evolving EKE spectrum. The two spectra match very well throughout the run, more so even during the later nonlinear stages. The EKE field initially lags the linear spectrum by a few time units, partly because we initialize the model with a zonal wavenumber which is much smaller than the most unstable one. However, the wavenumber cascade rate, the initial dominant wavenumber, and the final saturation wavenumber, are all predicted by the linear instability analysis. We also find an excellent match between the linear zonal phase speed and group velocity, and the actual phase and group progression of the interface waves (not shown).

This relation holds for other runs as well. Figure 8b shows the linear growth rate and EKE for a run with different parameter values — $\gamma = 1$, $\alpha = 0.5$, and $\hat{\beta} = 0.2$. In this run, there is a time period (roughly extending from $t = 5$ to 15) during which there is a secondary peak in the linear growth rate for long waves ($k \approx 3$). This secondary peak, even though it is relatively small, is also found in the EKE spectrum of the fully nonlinear run. Figure 9a shows the linear growth rate which corresponds to the mean flow during this period ($t = 7$). We see two peaks, at large and small wavenumbers. The meridional structures of the linear most unstable long-wave and short-wave modes ($k = 3$, $k = 12$) are shown in plots c,d. The long-wave mode is antisymmetric around the jet axis, with two peaks at the flanks of the jet, while the short-wave mode peaks in the middle of the jet, and is symmetric about the jet axis. The longitude-latitude structure of the meridional wind field from the nonlinear model run at this time (shown in plot b) fits the linear mode structure well, with a meridionally-symmetric wavenumber 12 in the center, and an antisymmetric wavenumber 3 structure at the jet flanks. This is so despite the highly-nonlinear filamentary structure of the PV field at this time (not shown). These results support the notion that linear instability organizes the flow field even during the nonlinear stages of the flow evolution. We note that nonlinear interactions contribute to the evolution of the zonal mean flow itself, so that the dynamics are not quasi-linear. However, given the mean flow, linear instability appears to determine the growth of each zonal wavenumber.

To further support this assertion, we compare the contributions of the linear and nonlinear terms to the EKE evolution. When deriving the domain-integrated energy equations from the Euler momentum equations, the Reynolds stress term $\langle -\overline{u'v'}\overline{u}_y \rangle$ (with overbar and angle brackets denoting zonal and meridional averages respectively) is the only contribution to energy growth, implying the domain-integrated contribution of the nonlinear terms is zero (Schmid and Henningson, 2001). Our QG model, however, does not make use of the Euler momentum equations (instead it is written in PV-streamfunction form), hence it requires a different approach to examining EKE.

Consider E_k (used earlier in Eq. 4):

$$E_k = \frac{1}{4}\left[u_k^* u_k + v_k^* v_k\right] . \tag{5}$$

Its time derivative is

$$\frac{\partial E_k}{\partial t} = \frac{1}{2}\left[u_k^* \frac{\partial u_k}{\partial t} + v_k^* \frac{\partial v_k}{\partial t}\right] . \tag{6}$$

We now use the geostrophic relation (Eq. 3), and the inverse Laplacian for the waves (Eq. 2 for $k \neq 0$) to relate the time derivative of the velocity components to that of the PV q,

$$\frac{\partial E_k}{\partial t} = \frac{1}{2}\left[-u_k^* \nabla_k^{-2}\left(\frac{\partial^2 q_k}{\partial y \partial t}\right) + ikv_k^* \nabla_k^{-2}\left(\frac{\partial q_k}{\partial t}\right)\right] \tag{7}$$

where ∇_k^{-2} is the inverse of the k^{th} Fourier component of the Laplacian ($\nabla_k^2 \equiv \frac{\partial^2}{\partial y^2} - k^2$), which we invert subject to periodic boundary conditions in x and zero meridional flow at the channel walls. We then use Eq. 1 to express the time derivative of PV, and thereby obtain a diagnostic expression for the time rate of change of E_k,

$$\frac{\partial E_k}{\partial t} = \frac{1}{2}\left[u_k^* \nabla_k^{-2}\left(\frac{\partial}{\partial y}\chi_k\right) - ikv_k^* \nabla_k^{-2}\chi_k\right] \tag{8}$$

where χ_k is the k^{th} component of the PV advection term, which when expressed in terms of linear and nonlinear components equals

$$\chi_k = ik\overline{u}q_k + v_k\overline{q}_y + ik(u'q')_k + \frac{\partial}{\partial y}(v'q')_k \, . \tag{9}$$

Here primes denote a deviation from the zonal mean. The first and second terms in Eq. 9 are the linear contributions to χ_k while the third and fourth terms are the nonlinear contributions.

Figure 10a shows the domain-integrated rate of change of EKE alongside the contributions of the linear and nonlinear terms. Also shown is the residual, calculated by subtracting the sum of the linear and nonlinear contributions from the full EKE terms, as an indication of the degree to which our diagnostic calculation is exact. Consistent with the theory, the domain integrated contribution of the linear terms essentially equals the total EKE growth, with the residual being on the order of 1% (ratio of variances). This 1% error is reasonable given the time discretization of the model output, as well as the fact that the PV anomaly fields which we use are a gridded version of the actual PV contours which are advected by the model at much higher resolution. Despite these errors, the domain-integrated nonlinear contributions are essentially zero (10^{-6}% of the variance).

While the nonlinear interactions do not contribute to the domain integrated EKE evolution, they do influence the spatial and spectral distribution of EKE. Figures 10c,d show wavenumber–time plots of the latitudinally-integrated contribution of the linear and nonlinear terms to E_k, plotted on top of the EKE spectrum, for the control run. The linear terms dominate the EKE production, but nonlinear wave–wave interactions persist when not integrated over all wavenumbers. These interactions act to spread the EKE to shorter waves at the expense of longer waves during the later stages of the evolution when the upscale energy cascade slows down (e.g. from wave numbers $3-4$ to $5-6$ after $t=15$ in the case shown).

Figures 10e,f show the spectrally-integrated contribution of the linear and nonlinear terms, as a function of time and latitude, plotted over the meridional distribution of EKE. The terms are calculated as in plots 10c,d, only here we sum over zonal wavenumbers rather than integrate meridionally. Again, we see a strong dominance of the linear terms, with the nonlinear terms acting to spread EKE from the central region containing the PV jumps to the jet flanks.

These findings indicate a dominant role for linear dynamics in determining the evolving wave structure. Nonlinear wave-wave interactions do not create EKE, rather they act to shift it in scale. It is important to note, however, that the linear stability analysis used to create figure 8 assumes a given zonal mean flow, which itself is evolving by nonlinear wave-wave interactions. Our results therefore do not imply that a wave-mean flow model will capture the full evolution well (consistent with Nielsen and Schoeberl, 1984).

5 Parameter sweep

In the previous section we described the flow evolution in terms of an initial linear growth stage, a nonlinear upscale cascade stage during which the PV gap narrows, and a final equilibrated stage, and noted that linear dynamics play an important role even in the nonlinear cascade stage. In this section we examine the full parameter sweep of runs. We find that the basic control run characteristics described in the previous sections hold across the entire parameter space considered. Here we examine quantitatively and qualitatively how quantities like the final domain-integrated EKE and wave amplitude depend on parameters, and thereby aim to elucidate the processes shaping the final flow equilibration.

5.1 General features of flow evolution and equilibration

We consider the full set of model runs, for which the strength of the negative PV strip is varied between 3 values ($\gamma = 0.5,\ 1,\ 2$), the initial gap width is varied between 4 values ($\alpha = 0,\ 0.5,\ 1,\ 2$) and β is varied between 5 values ($\hat{\beta} = 0,\ 0.05,\ 0.1,\ 0.15,\ 0.2$) — altogether 60 runs. Figure 11 shows the initial and final zonal mean zonal wind ($\overline{u}$) profiles for a representative subset of runs with $\hat{\beta} = 0,\ 0.1,\ 0.2$ and $\gamma = 0.5,\ 2$. We see that $\hat{\beta}$ has the largest effect on the initial $\overline{u}$, in particular, on the shape of the flow at the sides of the channel. For $\hat{\beta} \geq 0.1$ the shear reverses in the outer parts of the domain, with the extent of the reverse-shear regions and the strength of the shear increasing with $\hat{\beta}$. For all profiles, however, there is a locally eastward jet at the channel center, on which the instability develops and evolves. The effect of this instability on the zonal mean flow (shown in gray curves) is to weaken the eastward jet at the jet core (zonal deceleration), and to accelerate the flow slightly in the southern part of the domain. The weaker zonal mean winds at the jet core are partly a result of zonally averaging a wavy field — however, even the mean tangential winds along PV contours are weakened (not shown). The degree of change between the initial and final $\overline{u}$ profiles is mostly affected by γ, which directly controls the strength of the instability and its growth rate. The effect of α is mostly small, except for the case of $\hat{\beta} = 0.1$, $\gamma = 2$, where the different curves are well separated (we have not been able to explain what determines the sensitivity to α in this subset of runs).

While the initial zonal mean flow varies considerably with $\hat{\beta}$, the evolution of the disturbances as well as the zonal mean PV field vary remarkably little. Figure 12 shows the initial and final zonal mean PV fields, for the subset of runs with $\hat{\beta} = 0,\ 0.2$ and $\alpha = 0,\ 0.2$. For clarity, we show the profiles for 3 different γ values on each subplot. By comparing these plots, we see that γ affects the relative strength of the initial anti-cyclonic PV strip, while α slightly affects its meridional position. By construction, $\hat{\beta}$ does not affect the initial PV profile, but it does slightly affect the equilibrated profile (gray curves).

For all runs, the initial PV jump is smoothed out over a region of finite width, while the initial low-PV strip is mixed southwards, leaving a wide and shallow low PV region (c.f. figure 2b, and the gray curves in figure 12). The smoothing of the positive PV jump is a result of the zonal averaging of the wavy interface which actually remains sharp, and since the wave amplitudes increase with γ, the width of the smoothed out region increases with γ. The mixing of the anti-cyclonic PV strip, on the other hand, is the result of its breaking up into vortices, which merge and mix after being deformed by the strong cooperative shear ($\partial\bar{u}/\partial y > 0$) present between y_1 and y_2 (cf. figure 3). For weak to moderate PV strips ($\gamma \leq 1$), the vortices mix completely, leaving a smooth shallow low PV region. For $\gamma = 2$ and $\hat{\beta} \geq 0.1$, however, we see a small PV peak at the southern edge of the mixing region. In these runs (see for example the case $\alpha = 2$,

$\gamma = 2$, $\hat{\beta} = 0.2$ shown in figure 13), we find that the stronger vortices are able to withstand the shear, while they move downward due to a β-drift (Lam and Dritschel, 2001).

For $\hat{\beta} \geq 0.1$, the sign of the shear reverses about half way to the channel boundaries (e.g. see the black curve shown on the left side of figure 13a), and hence the vortices eventually run into a zone of adverse shear ($\partial\bar{u}/\partial y < 0$) which stretches them into filaments. Moreover, the elongated anti-cyclonic filaments become stable if the adverse shear becomes strong enough, resulting in a final zonal PV strip (e.g. figure 13d and the negative kinks in the final zonal mean PV profiles of figure 12). Dritschel (1989, p. 204) found by numerical experimentation that a periodic array of vortices will be stretched into filaments when the adverse shear exceeds approximately 21% of the anti-cyclonic PV anomaly (i.e. $-\partial\bar{u}/\partial y > 0.21\gamma\Delta q_0$). Using the initial mean velocity profile, $-\partial\bar{u}/\partial y = q_1 - \beta y$ in the southernmost region (see figure 1a) where $q_1 = \beta L_y/2 + \Delta q_0[(\gamma+1)w/L_y - 1]$, we find that this critical shear value of 21% occurs at latitude

$$y_{as} = \frac{L_y}{2} - w\frac{0.21\gamma + 1 - (1+\gamma)w/L_y}{\hat{\beta}} \,. \tag{10}$$

The solid horizontal lines in figure 13 show this latitude for the $\hat{\beta} = 0.2$ runs. We see that y_{as} well predicts the latitude where the vortices are elongated into filaments. The filaments forming south of y_{as}, where the adverse shear is stronger still, resist rolling back into vortices, even though the filaments are potentially unstable (Dritschel, 1989). However, this instability tends to fracture filaments into smaller filaments, and beyond $-\partial\bar{u}/\partial y \approx 0.64\gamma\Delta q_0$ even this instability is suppressed. The latitude at which this stronger shear occurs is marked by the dashed lines in figure 13d, and corresponds well to the location of the zonal PV filaments which form the kinks in figure 12. Taken together, these results underscore the key role played by adverse shear in barotropic instability when $\beta \neq 0$. Remarkably, results obtained using constant, spatially-uniform adverse shear in Dritschel (1989) well predict the shearing-out of the anticyclonic street of vortices produced in the early stages of instability, as well as the deposition of filamentary debris into a stable band at late times.

Next we examine the domain-integrated EKE (denoted $\|\mathrm{EKE}\|$) and show that it is closely related to the mean-square displacement $\overline{\eta^2}$ of the PV interface. This is expected given the dominance of the interface waves on the flow field structure (particularly evident after $t = 16$ in figure 3), and from the fact that the EKE-based zonal wavenumber k_e (Eq. 4) captures the interface wavenumber (rather than the number of vortices, which is sometimes slightly different, see e.g figure 13b). For the case of a single PV jump of magnitude $2\Delta q_0 = 4\pi$, in an infinite domain, the eddy PV anomaly is indeed dominated by the interface displacement, and can be related to it using Eq. 27 of Harnik and Heifetz (2007),

$$\|\mathrm{EKE}\|_{1\mathrm{J}} = \frac{(2\Delta \mathrm{q}_0)^2}{4\mathrm{k}}\overline{\eta^2} \tag{11}$$

where $\|\cdot\|$ and $\bar{\cdot}$ indicate integration over the entire domain and over the zonal direction, respectively, and the subscript $1J$ denotes a single jump (see appendix B for the explicit derivation). According to this relation, $\|\mathrm{EKE}\|$ is proportional to the wavelength times the root mean square (rms) interface displacement (which for a single wavenumber is twice the wave amplitude). From the discussion above, it is appropriate to take $k = k_e$.

To examine whether this relation — derived for a single PV interface — still holds in our model, we calculate the equilibrated $\|\mathrm{EKE}\|$, rms of interface displacement, and zonal wavenumber k_e, by time averaging each run over the final quarter of the integration ($37.5 \leq t \leq 50$). Figure 14 shows $\overline{\eta^2}/k$ as a function of $\|\mathrm{EKE}\|$, multiplied by a constant factor which we empirically found to give the best relation. The figure shows that indeed $\|\mathrm{EKE}\|$ is proportional to $\overline{\eta^2}/k$, but with a multiplicative factor $\pi/4$ (determined empirically) relative to Eq. 11:

$$\|\mathrm{EKE}\| = \frac{(\Delta \mathrm{q}_0)^2}{2\mathrm{k}}\overline{\eta^2}\frac{\pi}{2} = \frac{\pi}{4}\|\mathrm{EKE}\|_{1\mathrm{J}}\,. \tag{12}$$

This small difference may arise from the fact that we actually consider two jumps rather than one, in a confined channel rather than an open domain, which changes the Green function relation between PV and streamfunction.

This strong relation between $\|\mathrm{EKE}\|$ and $\overline{\eta^2}$ is a key new finding of the present study. The domain-integrated EKE is determined by two characteristic quantities of the flow: the average PV interface displacement and the characteristic zonal wavenumber. We expect this relation to hold well for other setups with a jet on a sharp PV jump, and for asymmetric barotropically unstable flows in which a sharp PV jump remains after the instability develops.

The relation between $\|\mathrm{EKE}\|$ and $\overline{\eta^2}$ also holds throughout the temporal evolution of individual runs, and not just for the equilibrated states. This is shown in figure 4a where $\overline{\eta^2}$ calculated every 5 time units is shown in stars. Examining the temporal evolution of $\|\mathrm{EKE}\|$, $\overline{\eta^2}$ and k_e for all other runs, we find that γ primarily influences the growth rate, the subsequent rate of vortex pairing, and the upscale energy cascade. In fact, $\gamma\Delta q$, which has units of PV, is the externally imposed evolution rate in this problem[1]. Fig 15 shows the time evolution of these quantities (with appropriate scaling, see below) for $\hat{\beta} = 0.5$ (plots a,b,c). Also shown (plot d) is $\|\mathrm{EKE}\|$ for $\hat{\beta} = 0.15$. We see that for a given $\hat{\beta}$, when we scale time by γ, the different curves nearly collapse on each other, with k_e clearly exhibiting a linear growth stage (during which the wavenumbers grow from the initially imposed wavenumber to the most unstable wavenumber), a nonlinear cascade stage, and a subsequent equilibration stage (figure 15a). $\|\mathrm{EKE}\|$ and $\overline{\eta^2}$ also increase with γ, since the growth rate increases with γ; however, the exact dependence is not as straightforward. In fact, empirically we find that for a given value of $\hat{\beta}$, the final mean-square interface displacement $\overline{\eta^2}$ scales best with γ (figure 15b), while the final $\|\mathrm{EKE}\|$ scales best with $\gamma^{3/2}$ (figure 15c,d). These results, along with Eq. 11, imply that the equilibrated interface wavenumber

[1] Strictly speaking, Δq — the magnitude of the positive jumps — is also an externally imposed evolution rate, but since we only vary the magnitude of the negative jump, $\gamma\Delta q$ is the relevant evolution rate for comparison between the different runs.

k_e should scale like $\gamma^{-1/2}$.

The dependence of $\|\text{EKE}\|$, $\overline{\eta^2}$ and k_e on $\hat{\beta}$ is more complicated than on γ and is even non-monotonic for smaller γ values. In the next section we develop an idealized model for the evolution and for the equilibrated state that is able to capture this relation. The dependence on α, denoted in the plots by different line thicknesses, is weak.

While the existence of a gap does not appreciably affect the basic relation between $\|\text{EKE}\|$ and interface wave amplitude, from the point of view of PV staircase formation it is worth examining how the change in gap width depends on the model parameters. Since the gap narrows when the anti-cyclonic vortices strip PV from it by filamentation, we expect the gap to be more affected by stronger vortices, which form more filaments. Figure 16 shows the relative change in gap width (with respect to the initial width) as a function of model parameters. We see, as expected, the strongest dependence on γ, with narrower final gaps for larger γ. We also see that narrower initial gaps (smaller α) are more affected, since the filaments form more readily on sharper PV profiles (Dritschel, 1988b), whereas $\hat{\beta}$ has little influence.

Additionally we examined a few parameter values outside the ranges indicated above to ensure that the main effects reported above are not qualitatively different. In particular, very wide gaps with $\alpha = 4$ did not result in significant differences from $\alpha = 2$. Very weak γ values (we examined $\gamma = 0.2$) result in very little disruption of the original jet, while very strong values (we examined $\gamma = 4$) give results qualitatively similar to $\gamma = 2$ except that a wider domain is needed to allow for equilibration, and the vortices do not mix completely (some smaller coherent vortices remain). Finally, values of $\hat{\beta} > 0.2$ greatly suppress the development of the initial instability by preventing meridional excursions of the anti-cyclonic vortices which initially roll up, thereby suppressing vortex pairing.

5.2 The mechanisms of flow equilibration

In common to all of the parameter sweep runs, an initially unstable zonal anti-cyclonic PV strip rolls up into vortices which shear and merge nonlinearly, while spreading southwards. During this process the interface waves grow in zonal wavelength and in amplitude, and this process continues as long as the zonal mean PV field is still linearly unstable. In this section we develop an idealized model of this process, and use it in combination with conservation laws to obtain a prediction of the final wave amplitudes, domain-integrated EKE, and some basic mean flow properties, all as a function of initial flow parameters.

Conservation of wave impulse is one of the basic laws governing the evolution of the flow. Dritschel (1988a) showed that for the contour dynamics model used here, this implies the conservation of the following wave activity quantity:

$$I = \frac{1}{2} \sum_j \Delta q_j \oint_{C_j} \eta_j^2 dx = const \tag{13}$$

where we sum the product of Δq_j — the PV jump across the j^{th} PV contour — and the integral along the contour C_j of the squared contour displacement η_j^2. Here, $\eta_j(x,t)$ is the displacement from its reference state latitude $\bar{y}_j$ (i.e. $y_j(x,t) = \bar{y}_j(y,t) + \eta_j(x,t)$), with $\bar{y}_j$ obtained by rearranging the flow into a zonally-symmetric, monotonically-increasing PV field — keeping the area between PV contours the same as in the actual flow state.

Examining the structure of the equilibrated flow in our runs, it is clear that implementing this wave activity conservation relation is practically impossible, given the high distortion and pinching off of the PV contours in the mixing region. We instead take an approximate, simpler approach. Ignoring the gap region, which has little influence on the final state, the equilibrated, non-zonal flow is taken to consist of three uniform-PV regions extending around the domain in the zonal direction, with highly-undulated boundaries separating them. The PV in the middle region is slightly lower than in the southern region, while that in the northernmost region is significantly larger, by an amount equal to the initial domain-wide jump ($q_4 - q_1 = 2\Delta q_0$). The undulations of the boundaries between these regions are a consequence of the initial barotropic instability, and since dissipation is negligible, they remain in the equilibrated state. We define a final "reference" state as the corresponding 3-region wave-free state, obtained by simply straightening the interfaces, so that no circulation is lost within a given region. This final reference state, shown in figure 1b, has only two PV jumps and is described by three unknown parameters: y_m, Δy_m and Δq_m, respectively the central latitude and width of the mixed region and the magnitude of the negative PV jump. Demanding that the domain-integrated PV be conserved yields

$$\Delta q_m = \frac{\gamma w \Delta q_0}{\Delta y_m} \tag{14}$$

for an initial state with $\alpha = 0$.

This idealized final state consists of only two contours, (1) at the main PV interface $y = y_{int} \equiv y_m + \frac{\Delta y_m}{2}$ where $\Delta q = 2\Delta q_0 + \Delta q_m$ and (2) at the southern edge of the mixing region $y = y_{sem} \equiv y_m - \frac{\Delta y_m}{2}$, and $\Delta q = -\Delta q_m$. This simplifies the application of Eq. 13 considerably so that

$$\overline{\eta_{int}^2} = -\frac{\Delta q_m}{2\Delta q_0 + \Delta q_m}\overline{\eta_{sem}^2} \approx -\frac{\Delta q_m}{2\Delta q_0}\overline{\eta_{sem}^2} \tag{15}$$

where for simplicity we neglect Δq_m relative to $2\Delta q_0$ (this is justified across the entire parameter space we have considered)[2]. In our numerical model runs, the main interface displacement η_{int} assumes a well-defined wavy shape, and its mean amplitude can be diagnosed simply using the PV contours which bound the gap region wrapping around the domain (black lines in figure 6). The southern interface y_{sem}, however, is not as clearly defined. While there is a clear lower edge to the mixed region (e.g. figure 3), it is not obviously associated with any single PV contour, since many of the contours in the mixed region close off to form vortices. We assume, for

[2] We here apply Eq. 13 to a *non-monotonic* reference state, which is permitted mathematically.

simplicity, that the messy mixed region can be replaced by a perfectly-mixed PV region with a wavy southern boundary, and that the amplitude of the waves on this boundary is proportional to the width of the mixing region: $\overline{\eta_m^2}^{1/2} = B\Delta y_m$ with a proportionality factor B to be determined empirically. Eqs. 15 and 14 then yield the following (scaled) estimate for the mean-square interface displacement:

$$\frac{\overline{\eta_{int}^2}}{w^2} = \frac{B^2\gamma\Delta y_m}{2w} . \tag{16}$$

Combining this with Eq. 12 further yields a relation between EKE and Δy_m:

$$\frac{\|\mathrm{EKE}\|}{\frac{\pi}{2}(w\Delta q_0)^2} = \frac{B^2\gamma\Delta y_m}{4kw} . \tag{17}$$

The validity of replacing the actual complex flow field by our highly-simplified model is our central assumption. In figures 17a,b we examine its validity by comparing $\overline{\eta_{int}^2}$ from Eq. 16 and $\|\mathrm{EKE}\|$ from Eq. 17, with the actual mean-square interface displacement and domain-integrated EKE of the equilibrated states of all 60 of our model runs. We find that a proportionality constant $B = \sqrt{2}$ gives the best fit. From both plots we see that for most runs, in particular those with smaller γ values, the implied theoretical relations between domain-integrated EKE and interface wave amplitude hold well in the nonlinear model. The run for which the EKE relation fits worst is $\gamma = 2$, $\alpha = 2$, $\hat{\beta} = 0$ (marked by a triangle added at the top of figure 17b). For this run, both large γ and zero $\hat{\beta}$ contribute to the spreading of the PV mixing region, which reaches the domain boundaries. Rerunning this case with a domain twice as wide ($L_y = \pi$) and recalculating the EKE-Δy_m relation yields an excellent scaling (marked by the large triangle at the top-right corner of figure 17b).

These results lend strong support to our simple conceptual model of flow equilibration, in which mixing by barotropic instability creates a final 3-region structure, under the constraints imposed by conservation of wave activity and circulation. The model provides a clear relation between the width of the mixed region and the final interface wave amplitude. Notably, our key assumptions (conservation of circulation and wave activity, along with Eq. 12) do not depend on y_m, the mean latitudinal position of the mixed region. In other words, the exact value of y_m does not matter in this simple model (it could in principle be determined by total energy conservation, but see below).

The width of the mixed region Δy_m in figure 17a,b, and the characteristic zonal wavenumber k_e in figure 17b, however, were determined *diagnostically* from each model run. Alternatively, we can use a linear stability analysis to determine Δy_m and k as follows. As the initial instability evolves and mixes PV, the width of the mixed region south of the initial jet increases. We saw in section 4 that this continues until the underlying zonal flow reaches a state of marginal stability. Using Eq. 14, and a linear stability analysis of the 3-region reference state (see appendix C for details), we find the maximum Δy_m which allows for instability, assuming (1) discrete zonal wavenumbers (consistent with x periodicity), and (2) that all the mixing occurs south of the initial interface location, so that $y_{int} = y_2 = (L_y + w)/2$ and correspondingly $y_m = (L_y + w + \Delta y_m)/2$. This latter assumption, which is both simple and well supported by the model runs (see figures 3 and 12), is elaborated below. We refer to the marginally unstable mixing region width as Δy_c (see Appendix C). The stability analysis *also* provides the wavenumber k for this marginally unstable flow. Figure 17c,d shows the relation between the computed values of $\overline{\eta^2}$ and $\|\mathrm{EKE}\|$ for the runs with $\alpha = 0$, and the corresponding estimates based on the marginally-unstable idealized profile (e.g. Eqs. 16 and 17 with Δy_c instead of Δy_m, and the corresponding wavenumber k). We see that this estimate works well, although it is not as quantitatively accurate as taking the actual edge of the mixing domain. In fact, a factor of $B = 2^{1/4}$ between $\overline{\eta^2}^{1/2}$ and Δy_c gives a much better fit. Nonetheless, a linear stability analysis yields a good qualitative prediction of how the final domain-integrated EKE and interface wave amplitudes depend on γ and $\hat{\beta}$.

6 Conclusions

In this work we comprehensively examined one of the most fundamental processes operating in the atmosphere and oceans: barotropic instability, which arises when both positive and negative PV gradients are present. Using a simple model generalizing the Rayleigh problem of a single PV strip to include a background meridional PV gradient in the simplest possible manner, we find a consistent pattern of behavior across a wide range of parameters defining the initial flow, beginning with a linear growth stage, a nonlinear cascade stage, and a subsequent equilibration stage.

The unstable perturbations mix the negative PV strip across a region which widens with time. Since circulation is conserved, the mean PV of the strip increases (becomes closer to zero). This process of widening and shallowing the low PV strip continues until the instability halts, leaving essentially the original large positive PV gradient, which now carries large-amplitude Rossby waves, alongside a shallow mixed low PV region. Conservation of wave activity then implies that the wave activity in the Rossby waves is equal to minus the wave activity embedded in the highly nonlinear mixed region.

To make the problem tractable, we then assume that the contribution of the PV contours in the highly distorted mixed region is equivalent to that of well defined waves on a single negative PV jump, with an amplitude which is directly related to the width of the mixed region. Since the interface waves dominate the non-zonal velocity field, their amplitude is an excellent measure of the domain-integrated EKE. Thus, by combining conservation of wave impulse and circulation, along with marginal linear stability, we obtain a model which links the final domain-integrated EKE to the width of the mixed region. The numerical integrations show that, across a very wide range of flow parameters, this theoretical model describes the equilibrated flow features particularly well given the actual width of the equilibrated mixed PV region, and describes it qualitatively well when the mixed region width is predicted from the *initial* mean flow parameters using marginal linear stability as an additional constraint.

We note that Schoeberl and Lindzen (1984), and also Nielsen and Schoeberl, (1984) used a similar approach for a barotropically unstable point jet, using enstrophy conservation and assuming the mean flow evolves to a neutrally stable state with PV rearrangement confined as much as possible to the jet center. Their implied final PV profile has uniform PV in the narrowest region possible, which requires averaging the PV between different zonal strips. Their assumption ignores however the impact of large amplitude waves, which act to broaden the region in which the PV gets mixed. One might argue that a more physical process is a rearrangement of PV to a monotonically increasing profile (c.f. Dritschel, 1988a). This was explicitly shown for the point jet problem by Shepherd (1988, figure 10) to be the nonlinear stability threshold for this problem, while the constant PV profile suggested by Schoeberl and Lindzen (1984) is the linear threshold. In the current profile (figure 1a), however, the lowest PV values are in the low PV strip, ruling out strict PV rearrangement (which requires the lowest PV values to be shifted to the lower domain edge). Rather, we find that the initial negative PV strip gets "diluted" by mixing with surrounding higher PV regions (mostly to its south). Correspondingly, the equilibrated PV profile is not monotonically increasing (e.g. Figs. 2b, 12, and 1b), though it *is* linearly stable. In short, we find that our initial, linearly-unstable PV profiles equilibrate far from their monotonically re-arranged profiles. This is not inconsistent with Dritschel (1988a), which simply proves that the re-arranged profile provides an upper bound on any instability. Equilibration can occur before this upper bound is reached.

A somewhat similar approach of combining basic conservation laws with assumptions on the mixing of PV in the equilibrated flow was used by Esler (2008) to study the equilibration of a 2-layer β-plane channel model, though he used energy instead of wave activity conservation (in addition to a constraint on potential energy which is irrelevant to the barotropic problem). In our problem, since we are not predicting the *actual* zonal-mean flow and wave structure, but rather a hypothetical mean flow and an idealized PV interface wave, we replace the turbulent mixed region south of the main PV interface by a second, weaker PV interface. This greatly simplifies the wave activity conservation relation, which makes it much easier to use than energy conservation. Our main purpose, we emphasize, has been to elucidate general characteristics of nonlinear flow equilibration by means of the simplest relevant physical model.

The idealized flow studied in this paper has allowed a detailed study of various other processes related to the growth and saturation of barotropic instability, including the underlying mechanisms of wave growth, scale cascade, vortex drift, vortex shearing, PV mixing, staircase formation, and the stabilizing role of adverse shear. The original motivation for this work was to better understand the process of zonal acceleration by PV mixing (leading to jet sharpening), when the waves are internally generated by the barotropic instability mechanism, rather than externally imposed as in Dritschel and Scott (2010). In fact, we have found barotropic instability to be an *inefficient* mechanism for jet sharpening. This instability typically leads to a zonal flow *deceleration*. This is primarily due to the initial strong deceleration caused by eddy growth, during which the PV flux is predominantly down gradient. Up-gradient flux still occurs on the flanks of the jet, mainly on the northern flank, resulting in local jet sharpening (enhanced PV gradients), but rarely enough to counteract the deceleration occurring in the initial stages of barotropic instability.

A key finding obtained from our extensive simulation results is that the dominant length scales which emerge are tightly controlled by the linear instability of the instantaneous zonal mean flow, even though the mean flow itself changes only through nonlinear interactions. This control applies at all times, not just during the initial linear growth stage, but also as the flow equilibrates (and stabilizes). A noteworthy feature resulting from the dominance of wave dynamics is the highly inhomogeneous structure of the enstrophy cascade; while we find enstrophy to cascade predominantly downscale through filamentation, as in classical homogeneous two-dimensional turbulence, part of the enstrophy remains trapped in the wavy jet and cascades *upscale*, along with eddy kinetic energy. The waves themselves on the jet are induced by the anti-cyclonic eddies formed in the initial instability stages. These eddies drift southwards, interact, shed PV, and eventually get sheared out completely in most cases, leaving a well-mixed, stable mean PV structure.

An important feature of our model problem is a mean PV gradient which cannot be broken down by the flow instability, but is rather re-shaped by it. This differs strongly from the classical Rayleigh problem where the vortex strip breaks into vortices which interact and spread limitlessly into the flow domain, with no background gradient to hold them back. In our model problem, and the related one studied by Nielsen and Schoeberl (1984), a very different evolution takes place in which waves play a much more important role, to the extent that linear theory guides the course of the flow evolution at all times, even at later evolution stages when the flow equilibrates (and stabilizes). Nonlinearity does the work of modifying the background state upon which the waves propagate. In particular, the dominant length scales which emerge are tightly controlled by the linear instability of the instantaneous zonal mean flow, even though the mean flow itself changes only through nonlinear interactions. Arguably, this behaviour is more generally applicable wherever mean-flow gradients persist through instability[3].

A noteworthy feature resulting from the dominance of wave dynamics is the highly inhomo-

[3]For example, in the Holmboe problem, instability arises from the interaction of a vorticity wave on a shear-generated vorticity gradient, with a gravity wave on a near-by density interface (Umurhan and Heifetz, 2007). In analogy to our problem, we expect the gravity interface to survive the instability, and the gravity waves arising on it to organize the flow during the non-linear evolution.

geneous structure of the enstrophy cascade; while we find enstrophy to cascade predominantly downscale through filamentation, as in classical homogeneous two-dimensional turbulence, part of the enstrophy remains trapped in the wavy jet and cascades *upscale*, along with eddy kinetic energy. The waves themselves on the jet are induced by the anti-cyclonic eddies formed in the initial instability stages. These eddies drift southwards, interact, shed PV, and eventually get sheared out completely in most cases, leaving a well-mixed, stable mean PV structure with waves.

In closing, a unique aspect of our study is the application and validation of a new, simple theoretical model to a very wide range of barotropically-unstable PV profiles. Given the various simplifications and assumptions made, the ability of the theoretical model to predict the dependence of the fully nonlinear equilibrated state on the initial flow parameters is particularly remarkable. In future work, we will address the effect of a finite Rossby deformation length, and of a background mean shear. Additionally, we are currently generalizing this study to a more realistic two-layer system to examine the competition between barotropic and baroclinic instability, as well as their equilibration.

Acknowledgements DGD is grateful for the support received through a Leverhulme Trust Research Fellowship, which greatly facilitated the collaboration underpinning this research. We thank Jonas Nycander, Ted Shepherd, Gavin Esler, and an anonymous reviewer for their comments and suggestions which helped improve the manuscript and theoretical model. NH and EH acknowledge support received by the Israeli Science Foundation grants 1084/06, 1370/08, 1537/12. EH is grateful to the International Meteorological Institute (IMI) of Stockholm University for hosting him at the Meteorological Institute of Stockholm University (MISU)

Appendix A: The numerical method

The numerical simulations were performed using the Combined Lagrangian Advection Method (CLAM, Dritschel and Fontane (2010)), a highly-accurate hybrid method based on contour advection (Dritschel and Ambaum, 1997) and standard pseudo-spectral techniques. The method achieves high accuracy by representing advected tracers, here the PV, principally as (grid-free) material contours down to scales as small as a sixteenth of the basic 'inversion' grid size. The inversion grid is used to invert Laplace's operator in (2) and obtain the velocity in (3). The PV contours move through the grid, obtaining their velocity as needed by interpolation. Dissipation is carried out by 'contour surgery', which removes thin filaments and join close contours of the same PV level. This greatly reduces the effective dissipation compared to other standard methods — see Dritschel and Scott (2009) for a recent comparison.

The simulations all use a basic inversion grid of dimensions 1024 in x and 256 in y, corresponding to 3.2 grid points across the anti-cyclonic zone (whose width is fixed at $w = L_y/40 = \pi/80$). Even half of this resolution in each direction is adequate to resolve the flow evolution in detail, but the higher resolution used here improves the calculation of various diagnostics, described below. To induce instability, a small perturbation is added to the 'latitude' y_2 of the central jump. For each x grid point x_i, first a random displacement $\eta_i \in [-1, 1]$ is generated. This is then spread by applying 400 1-2-1 local averages: $(\eta_{i-1} + 2\eta_i + \eta_{i+1})/4 \mapsto \eta_i$. This correlates the perturbation over approximately 20 grid lengths in x (of the 1024). Finally, the η_i are scaled so that $\mathsf{max}|\eta_i| = 0.1w$. This procedure results in a random long-wave disturbance having a much larger scale than the primary modes of instability. Nonlinear interactions subsequently generate shorter waves, exciting instability — without enforcing a single scale — thereby enabling secondary instabilities and so on. The main features occurring in the time evolution, as well as the flow equilibration, are not sensitive to the details of the initial disturbance.

The piecewise-uniform gridded PV field is then constructed on an ultra-fine grid (16 times finer than the inversion grid) in y. This is then averaged back to the inversion grid by successive 1-2-1 averages (Dritschel and Ambaum, 1997), resulting in a slightly smoothed PV distribution. This smoothed distribution is then contoured using a fast contouring algorithm (Dritschel and Ambaum, 2006). Here, one needs to specify a fixed contouring interval δq, and in this study we have chosen $\delta q = \Delta q_0/16$, so that each jump in the double jet is represented by 16 contours. One might wonder why a single contour is not sufficient. The reason is that mixing following Rossby-wave breaking is poorly represented by a single contour; the numerical method (CLAM) is designed to accurately represent this mixing by using many contours and co-evolving a pair of gridded PV fields on the inversion grid that compensate for contour dissipation, as discussed in detail in Fontane and Dritschel (2009) and Dritschel and Fontane (2010). The remaining numerical parameters are those set out in Fontane and Dritschel (2009), who resolved all parameter interdependencies, in particular the dependence of contour resolution on the grid resolution. CLAM uses a 4th-order Runge-Kutta time stepping scheme with an adaptive time step Δt chosen to ensure both $\mathsf{max}|q'|\Delta t < \pi/10$ and $\mathsf{max}|\boldsymbol{u}|\Delta t/\Delta x < 0.7$, the latter CFL condition required in the pseudo-spectral part of the code.

Appendix B: Derivation of Eq. 11

The domain integrated energy per unit zonal wavelength can be written as:

$$\|\mathrm{EKE}\| = -\frac{1}{2\lambda}\int_{\mathrm{y}=-\infty}^{\infty}\int_{\mathrm{x}=0}^{\lambda}\psi \mathrm{q}\mathrm{d}\mathrm{x}\mathrm{d}\mathrm{y}\,. \tag{18}$$

For a single vorticity jump interface, $\partial\overline{q}/\partial y = \Delta\overline{q}\delta(y - y_{1j})$, and the linearization of Eq. 2 yields

$$q = \nabla^2\psi = -\eta\Delta\overline{q}\delta(y - y_{1j})\,. \tag{19}$$

Hence, for a wave-like solution of the form $\eta = A(t)e^{i(kx+\epsilon(t))}$, the open domain Green function satisfies

$$\nabla^2 G(y, y_{1j}) = -k^2 G + \frac{\partial^2 G}{\partial y^2} = -\frac{e^{-k|y-y_{1j}|}}{2k} \tag{20}$$

so that

$$\psi = \frac{\Delta\overline{q}}{2k} e^{-k|y-y_{1j}|} \eta\,. \tag{21}$$

Substituting Eqs. 19 and 21 back into Eq. 18 gives:

$$\|\mathrm{EKE}\|_{1\mathrm{j}} = \frac{(\Delta\overline{\mathrm{q}})^2 \overline{\eta^2}}{4\mathrm{k}} \int_{\mathrm{y}=-\infty}^{\infty} \mathrm{e}^{-\mathrm{k}|\mathrm{y}-\mathrm{y}_{1\mathrm{j}}|} \delta(\mathrm{y}-\mathrm{y}_{1\mathrm{j}}) \mathrm{dy} = \frac{(\Delta\overline{\mathrm{q}})^2 \overline{\eta^2}}{4\mathrm{k}} \tag{22}$$

which is Eq. 11.

Appendix C: Calculation of Δy_c from linear stability

In our theoretical model presented in section 5.1, we explained that linear stability may be used to estimate the width of the mixed zone $\Delta y_m = \Delta y_c$ between $y_{sem} \equiv y_m - \frac{\Delta y_m}{2}$ and $y_{int} \equiv y_m + \frac{\Delta y_m}{2}$ in our idealized reference state (see figure 1b), consisting of three uniform regions of PV, $q = q_1$, $q_1 - \Delta q_m$ and $q_1 + 2\Delta q_0$, where $\Delta q_m = \gamma w \Delta q_0 / \Delta y_m$ from Eq. 14. The stability analysis is straightforward: one displaces the undisturbed interfaces at $y = y_{sem}$ and y_{int} by infinitesimal perturbations η_{sem} and η_{int} proportional to $\exp\{\mathrm{i}(kx - \sigma t)\}$ where k is the wavenumber and σ is the frequency (the imaginary part giving the growth rate). Using the fact that each interface is material ($\mathrm{D}\eta/\mathrm{D}t = v$) yields a pair of algebraic equations

$$\mathrm{i}(k\overline{u}(y_{sem}) - \sigma)\hat{\eta}_{sem} = \hat{v}(y_{sem}) \tag{23}$$

$$\mathrm{i}(k\overline{u}(y_{int}) - \sigma)\hat{\eta}_{int} = \hat{v}(y_{int}) \tag{24}$$

where hats are used on the complex amplitudes of the fields (i.e. stripped of the $\exp\{\mathrm{i}(kx-\sigma t)\}$ phase factor, which cancels in the linearized equations). The mean zonal velocities are given by

$$\overline{u}(y_{sem}) = \frac{1}{2}\beta y_{sem}^2 - q_1 y_{sem} \tag{25}$$

$$\overline{u}(y_{int}) = \frac{1}{2}\beta y_{int}^2 - q_2 y_{int} + \Delta q_m y_{sem} \tag{26}$$

where $q_2 \equiv q_1 - \Delta q_m$. The remaining algebraic equations are found from applying continuity of velocity at the interfaces and requiring $v = 0$ at the domain edges, $y = 0$ and L_y. Continuity of the zonal velocity at the *perturbed* interfaces yields, after linearization and cancellation of the phase factor,

$$-\Delta q_m \hat{\eta}_{sem} = [\hat{u}](y_{sem}) \tag{27}$$

$$(2\Delta q_0 + \Delta q_m)\hat{\eta}_{int} = [\hat{u}](y_{int}) \tag{28}$$

where $[f](y)$ denotes the jump in a quantity f crossing $y =$ constant from below. Finally, the forms of $\hat{u}(y)$ and $\hat{v}(y)$ are obtained by solving Laplace's equation $\mathrm{d}^2\hat{\psi}/\mathrm{d}y^2 - k^2\hat{\psi} = 0$ in each of the three uniform PV regions, matching $\hat{\psi}$ across each undisturbed interface (this is equivalent to matching $\hat{v}$ since $\hat{v} = \mathrm{i}k\hat{\psi}$ and here we consider only $k > 0$), and requiring $\hat{\psi} = 0$ at the domain edges (details omitted). Note that $\hat{u} = -\mathrm{d}\hat{\psi}/\mathrm{d}y$.

The algebraic equations obtained have a non-trivial solution only if σ takes one of two (eigen)values:

$$\sigma = \frac{a_{11} + a_{22} \pm \sqrt{(a_{11}+a_{22})^2 + 4(a_{12}a_{21} - a_{11}a_{22})}}{2} \tag{29}$$

where

$$a_{11} = \overline{u}(y_{sem}) + s_1\left(b_0 e^{\kappa y_{sem}} - b_2 e^{-\kappa y_{sem}}\right) \tag{30}$$

$$a_{22} = \overline{u}(y_{int}) - b_1 s_2\left(e^{\kappa y_{int}} - e^{-\kappa y_{int}}\right) \tag{31}$$

$$a_{12} = -b_1 s_2\left(e^{\kappa y_{sem}} - e^{-\kappa y_{sem}}\right) \tag{32}$$

$$a_{21} = s_1\left(b_0 e^{\kappa y_{int}} - b_2 e^{-\kappa y_{int}}\right) \tag{33}$$

where $\kappa \equiv kL_y$, $s_1 = -\Delta q_m \sinh(\kappa y_{sem})/\kappa$, $s_2 = (2\Delta q_0 + \Delta q_m)\sinh(\kappa(L_y - y_{int}))/\kappa$, $b_0 = (e^{2\kappa} - 1)^{-1}$, $b_1 = b_0 e^{\kappa}$ and $b_2 = b_0 e^{2\kappa}$. If the expression inside the square root for σ is negative, the flow is unstable, and the growth rate is given by the imaginary part of σ, denoted σ_{i} (the positive sign corresponding to growth, and the negative sign corresponding to decay).

The objective of this analysis is to determine the smallest width of the mixed zone, $\Delta y_m = \Delta y_c$, for which the flow is stable for all permissible wavenumbers k (here positive integer values). This requires finding the marginal stability boundary, namely where $(a_{11} + a_{22})^2 + 4(a_{12}a_{21} - a_{11}a_{22}) = 0$, for each k. We have chosen to fix $y_{int} = (L_y + w)/2$ (the original location of the positive PV jumps for a zero gap width, see figure 1b), since the mean location of y_{int} is not observed to shift significantly in any of our 60 model runs. We then increased Δy_m progressively from w (as in the original setup) until marginal stability is found at $\Delta y_m = \Delta y_c$. Figure 18 shows the typical behaviour of the growth rate σ_{i} (scaled by Δq_0, plot a) and the most unstable wavenumber k (the number of waves which fit into the domain, plot b), as a function of the mixed region width, for the case $\gamma = 1$ and $\hat{\beta} = 0.1$. A difficulty is that the margin of stability is generally not unique. To circumvent this, we have instead defined marginal stability to be the point where $\sigma_{\mathrm{i}} = \sigma_{\mathrm{min}}$, a small fraction of Δq_0, since typically very weak growth rates are insufficient to produce nonlinear disruption of the flow. In the results reported, we have used $\sigma_{\mathrm{min}} = 0.01\Delta q_0$ (horizontal dashed line in figure 18a). This would place the margin of stability at $y_{sem} = 0.1815L_y$, with a zonal wavenumber 5 (marked by circles in figure 18) in this case. Other choices for the stability margin yield qualitatively similar results.

References

Cohen NY, Gerber EP, Buhler O (2013) Compensation between resolved and unresolved wave driving in the stratosphere: Implications for downward control. J Atmos Sci In press

Dritschel DG (1988a) Nonlinear stability bounds for inviscid, two-dimensional, parallel or circular flows with monotonic vorticity, and the analogous three- dimensional quasi-geostrophic flows. J Fluid Mech 191:575–582

Dritschel DG (1988b) The repeated filamentation of two-dimensional vorticity interfaces. J Fluid Mech 194:511–547

Dritschel DG (1989) On the stabilization of a two-dimensional vortex strip by adverse shear. J Fluid Mech 206:193–221

Dritschel DG, Ambaum MHP (1997) A contour-advective semi-lagrangian numerical algorithm for simulating fine-scale conservative dynamical fields. Quart J Roy Meteorol Soc 123:1097–1130

Dritschel DG, Ambaum MHP (2006) The diabatic contour advective semi-lagrangian algorithm. Mon Wea Rev 134:2503–2514

Dritschel DG, Fontane J (2010) The combined lagrangian advection method. J Comput Phys 229:5408–5417

Dritschel DG, McIntyre ME (2008) Multiple jets as PV staircases: the Phillips effect and the resilience of eddy-transport barriers. J Atmos Sci 65:855–874

Dritschel DG, Scott RK (2009) On the simulation of nearly inviscid two-dimensional turbulence. J Comp Phys 228:2707–2711

Dritschel DG, Scott RK (2010) Jet sharpening by turbulent mixing. Phil Trans Roy Soc 369:754–770

Dritschel DG, Scott RK, Macaskill C, Gottwald G, Tran C (2009) Late time evolution of unforced inviscid two-dimensional turbulence. J Fluid Mech 640:215–233

Eliassen A, Palm E (1961) On the transfer of energy in stationary mountain waves. Geophys Publ 22:1–23

Esler JG (2008) The turbulent equilibration of an unstable baroclinic jet. J Fluid Mech 599:241–268

Ferreira RN, Schubert WH (1997) Barotropic aspects of ITCZ breakdown. J Atmos Sci 54:261–285

Fjørtoft R (1953) On the changes in the spectral distribution of kinetic energy for twodimensional, nondivergent flow. Tellus 5:225–230

Fontane J, Dritschel DG (2009) The hypercasl algorithm: a new approach to the numerical simulation of geophysical flows. J Comput Phys 228:6411–6425

Harnik N, Heifetz E (2007) Relating over-reflection and wave geometry to the counter propagating rossby wave perspective: Toward a deeper mechanistic understanding of shear instability. J Atmos Sci 64:2238–2261

Haynes PH (1985) Nonlinear instability of a rossby-wave critical layer. Journal of Fluid Mechanics 161:493–511

Haynes PH (1989) The effect of barotropic instability on the nonlinear evolution of a rossby-wave critical layer. J Fluid Mech 207:231–266

Hoskins BJ, McIntyre ME, Robertson AW (1985) On the use and significance of isentropic potential-vorticity maps. Quart J Roy Meteorol Soc 111:877–946.

Ingersoll AP, Dowling TE, Gierasch PJ, Orton GS, Read PL, Sanchez-Lavega A, Showman AP, Simon-Miller AA, Vasavada AR (2004) Dynamics of Jupiter's atmosphere, Cambridge Univ. Press, pp 105–128

Kuo HL (1949) Dynamic instability of two-dimensional nondivergent flow in a barotropic atmosphere. J Atmos Sci 6:105–122

Lam JSL, Dritschel DG (2001) On the beta-drift of an initially circulat vortex patch. J Fluid Mech 436:107–129

Marcus PS (1993) Jupiter's great red spot and other vortices. Ann Rev Astron Astrophys 31:523–573

McIntyre ME (1994) The quasi-biennial oscillation (QBO): some points about the terrestrial QBO and the possibility of related phenomena in the solar interior. In: Nesme-Ribes E (ed) In: The Solar Engine and its Influence on the Terrestrial Atmosphere and Climate (Vol. 25 of NATO ASI Subseries I, Global Environmental Change), Heidelberg, Springer-Verlag, pp 293–320

Nielsen JE, Schoeberl MR (1984) A numerical simulation of barotropic instability. part ii: wave-wave interaction. J Atmos Sci 41:2869–2881

Panetta RL (1993) Zonal jets in wide baroclinically unstable regions: Persistence and scale selection. J Atmos Sci 50:2073–2106

Rayleigh L (1880) On the stability, or instability, of certain fluid motions. Proc London Math Soc 9:57–70

Rhines PB (1975) Waves and turbulence on a beta-plane. J Fluid Mech 69:417–443

Rogers JH (1995) The Giant Planet Jupiter. Cambridge, University Press

Schmid PJ, Henningson DS (2001) Stability and Transition in Shear Flows. Springer

Schoeberl MR, Lindzen RS (1984) A numerical simulation of barotropic instability. part I: wave-mean flow interaction. J Atmos Sci 41:1368–1379

Scott RK, Dritschel DG (2012) The structure of zonal jets in geostrophic turbulence. Journal of Fluid Mechanics 711:576–598

Shepherd TG (1988) Rigorous bound on the nonlinear saturtion of instabilities to parallel shear flows. J Fluid Mech 196:291–322

Umurhan OM, Heifetz E (2007) Holmboe modes revisited. Phys Fluids 19:064,101

Vallis GK (2006) Atmospheric and Oceanic Fluid Dynamics. Cambridge University Press, Cambridge, U.K.

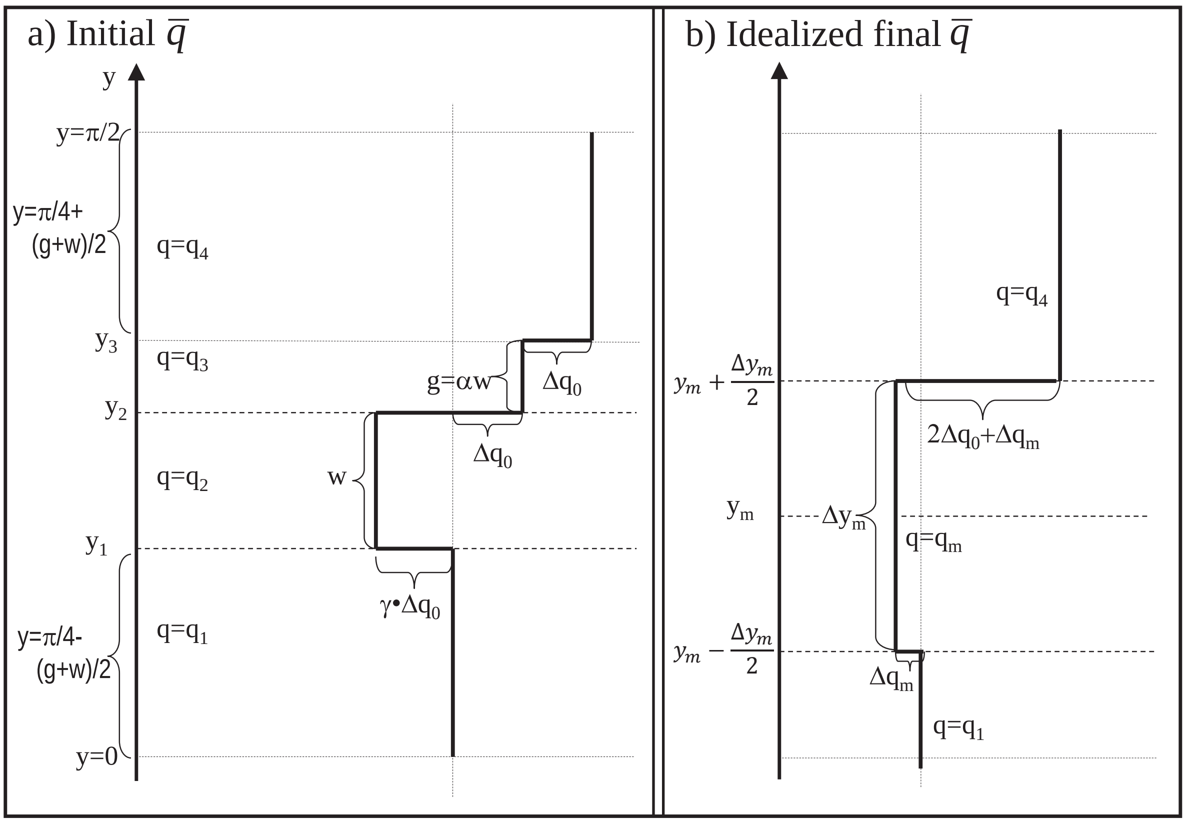

Figure 1: The basic-state PV structure together with the relevant parameters defining it: a) the initial zonally symmetric state. b) an idealized equilibrated state, as discussed in Sec. 5.2.

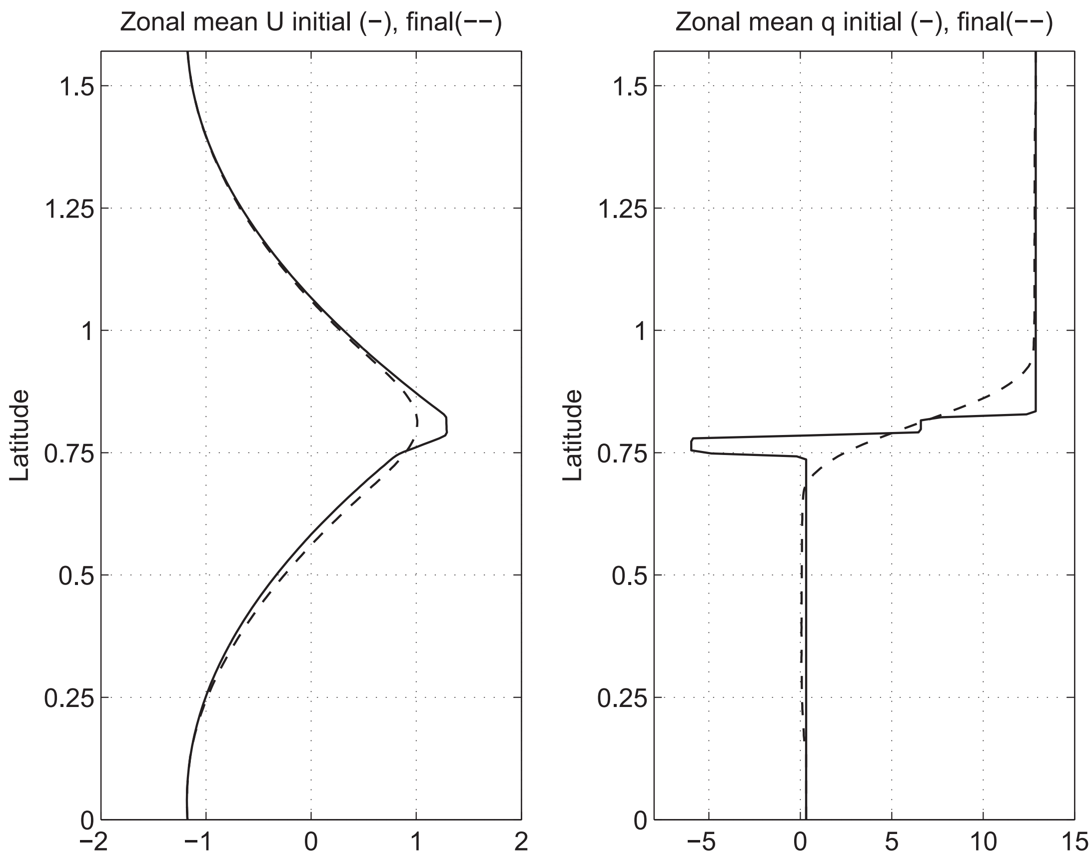

Figure 2: The initial (solid) and final (time $t = 50$, dashed) zonally-averaged profiles of a) zonal wind and b) PV, for the control run ($\alpha = 1$, $\gamma = 1$, $\hat{\beta} = 0.05$).

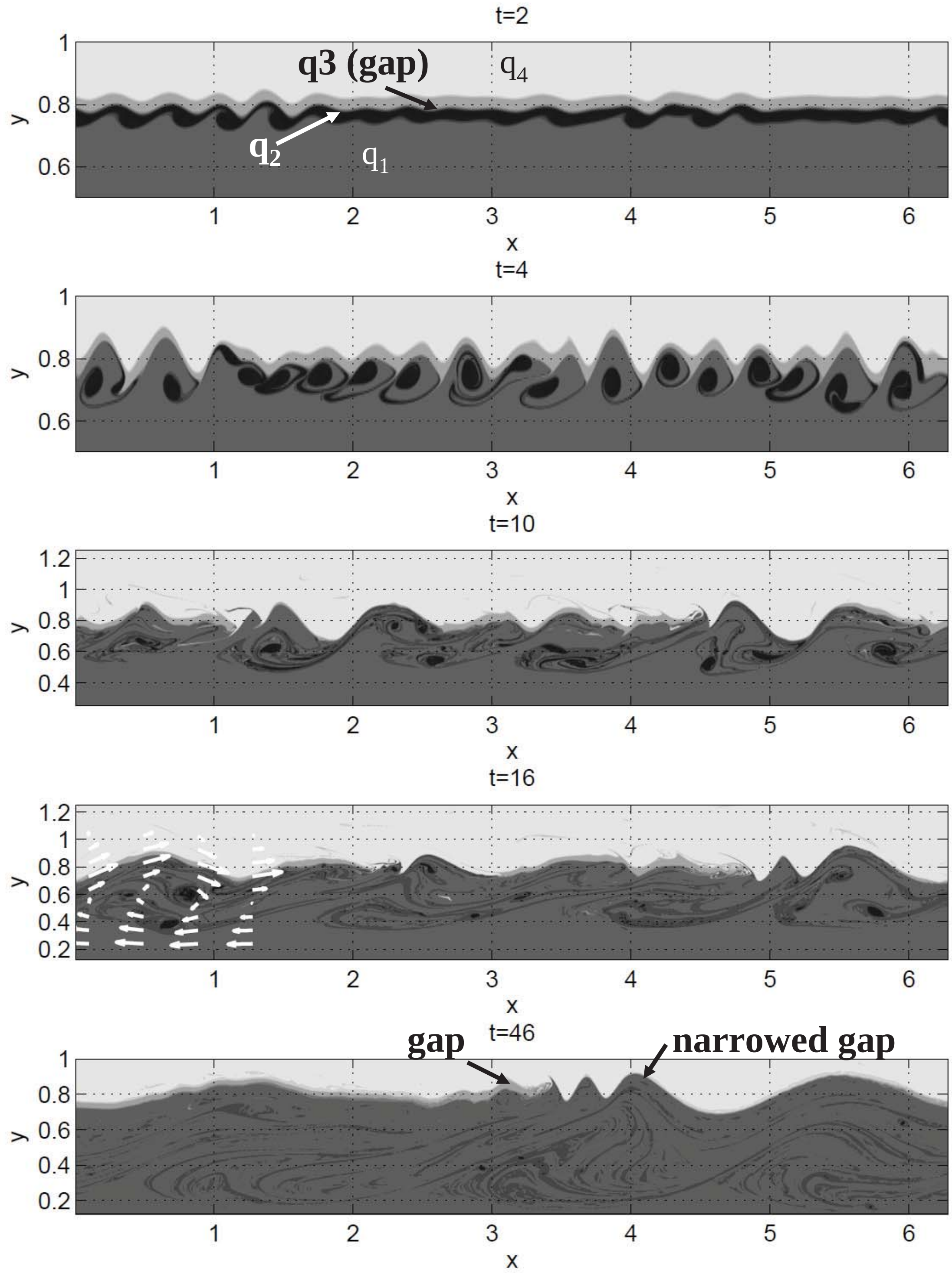

Figure 3: x-y snapshots of the PV field which starts from a zonally-symmetric profile as in figure 1, at times $t = 2,\ 4,\ 10,\ 16,\ 46$ (gray shading). The low PV strip, q_2 (darkest shading in top plot), breaks up into low PV vortices. The gray shading denotes the four PV values of figure 1a, marking q_2, q_1, q_3, q_4 from darkest to brightest gray, respectively. The white arrows shown in $t = 16$ indicate the flow in the x-y plane. Note that the latitude range shown varies between the plots.

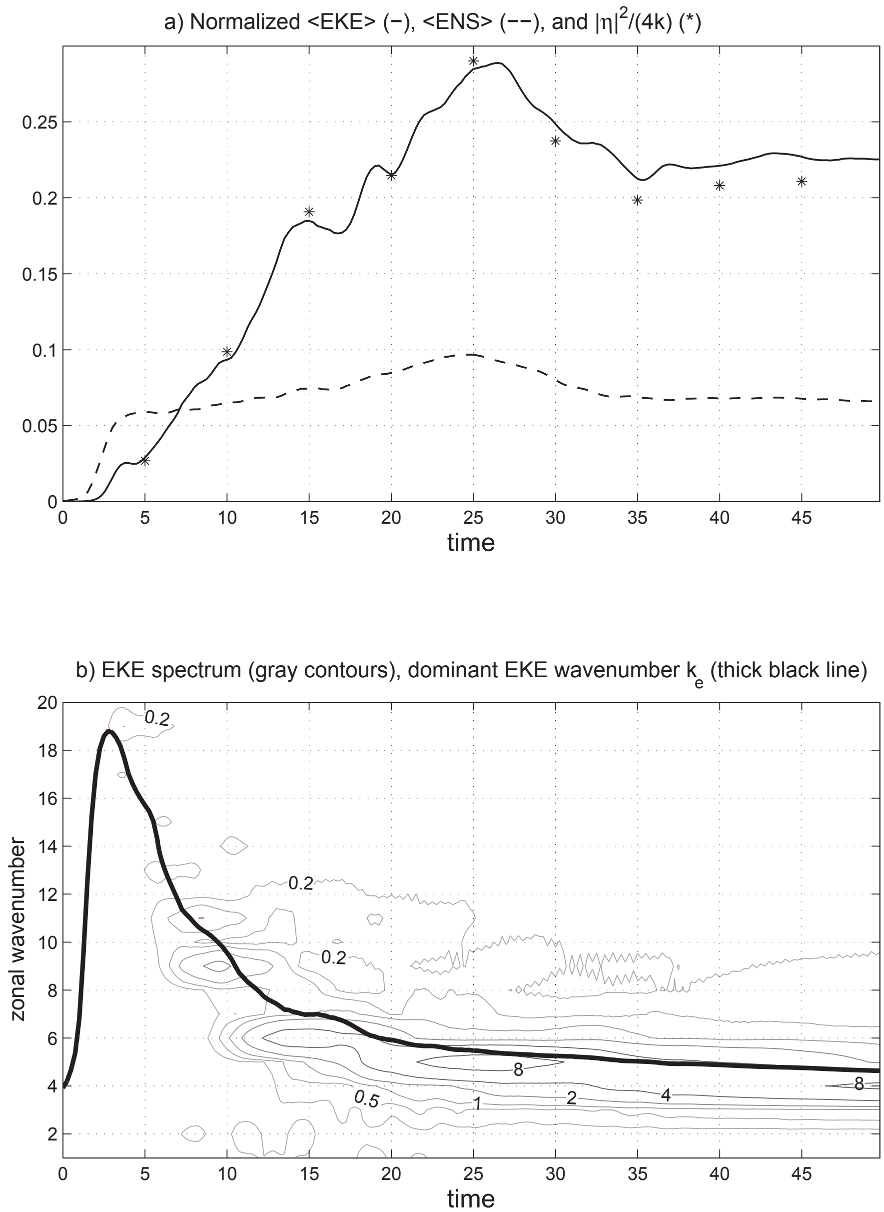

Figure 4: a) Domain-integrated EKE (times 10, solid line) and eddy enstrophy (dashed line), normalized by $(w\Delta q_0)^2$, and the correspondingly scaled mean squared interface displacement (see Eq. 12), at every 5 time units. b) EKE spectrum (thin contours), and the dominant energy wavenumber k_e (Eq. 4, thick black line).

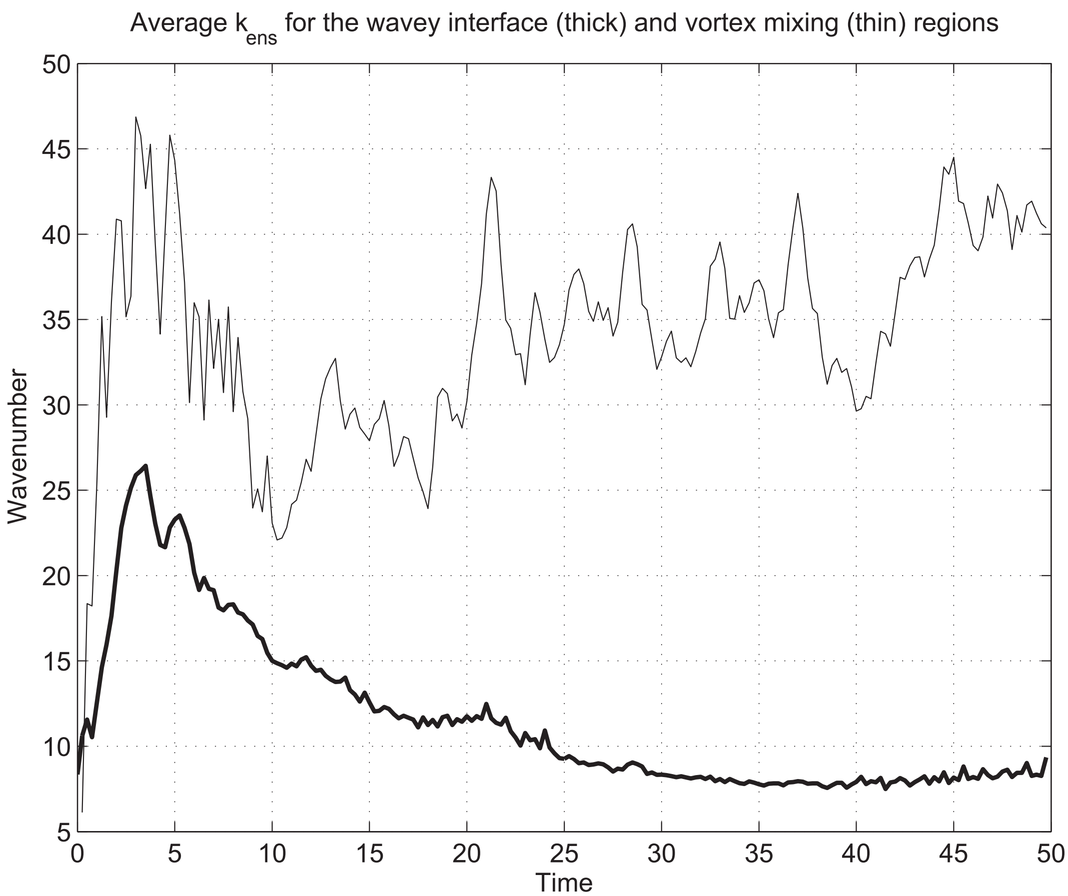

Figure 5: The dominant enstrophy wavenumber k_{ens} (as in Eq. 4, but with enstrophy instead of EKE) averaged over the region in which the negative PV vortices dominate ($0.3 \leq y \leq 0.6$, thin line) and over the region dominated by the interface ($0.7 \leq y \leq 0.9$, thick line).

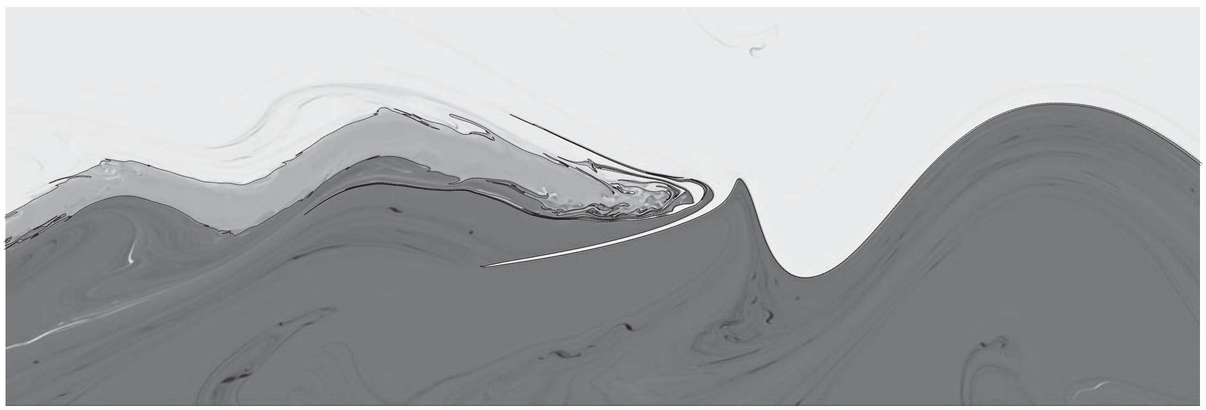

Figure 6: An example of the “dragon-head” structure which forms in the PV field (shaded as in figure 3), taken from $t = 25$ in the control run. The two PV contours which wrap the domain at the two edges of the gap are marked with a thin black line. The mean distance between these two wrapping contours is calculated for each longitude section, and then averaged to produce the gap-width statistics of figure 7.

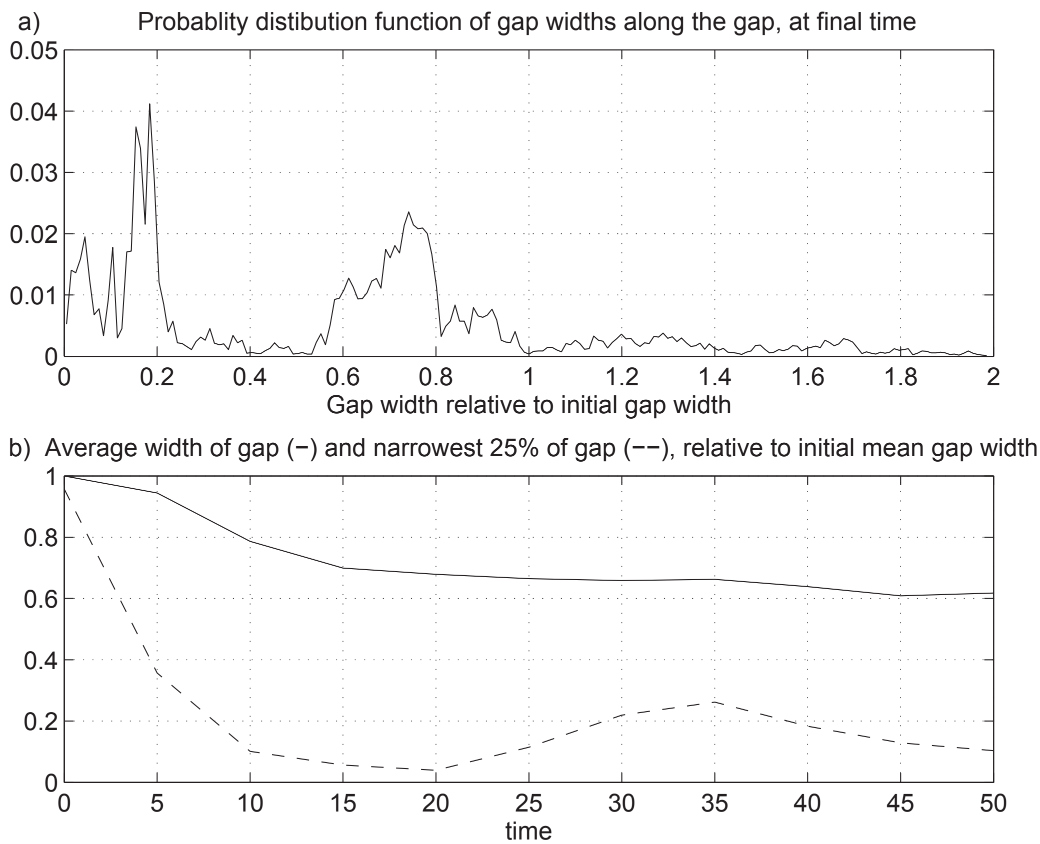

Figure 7: a) The probability distribution function of the different gap width values along a latitude circle at the final time of the control run. b) The time evolution of average gap width of all longitude sections (solid) and the narrowest 25% of longitude sections (dashed). The gap statistics are calculated at every 5 units of time. In both plots, the gap width is given as a fraction of the initial gap width.

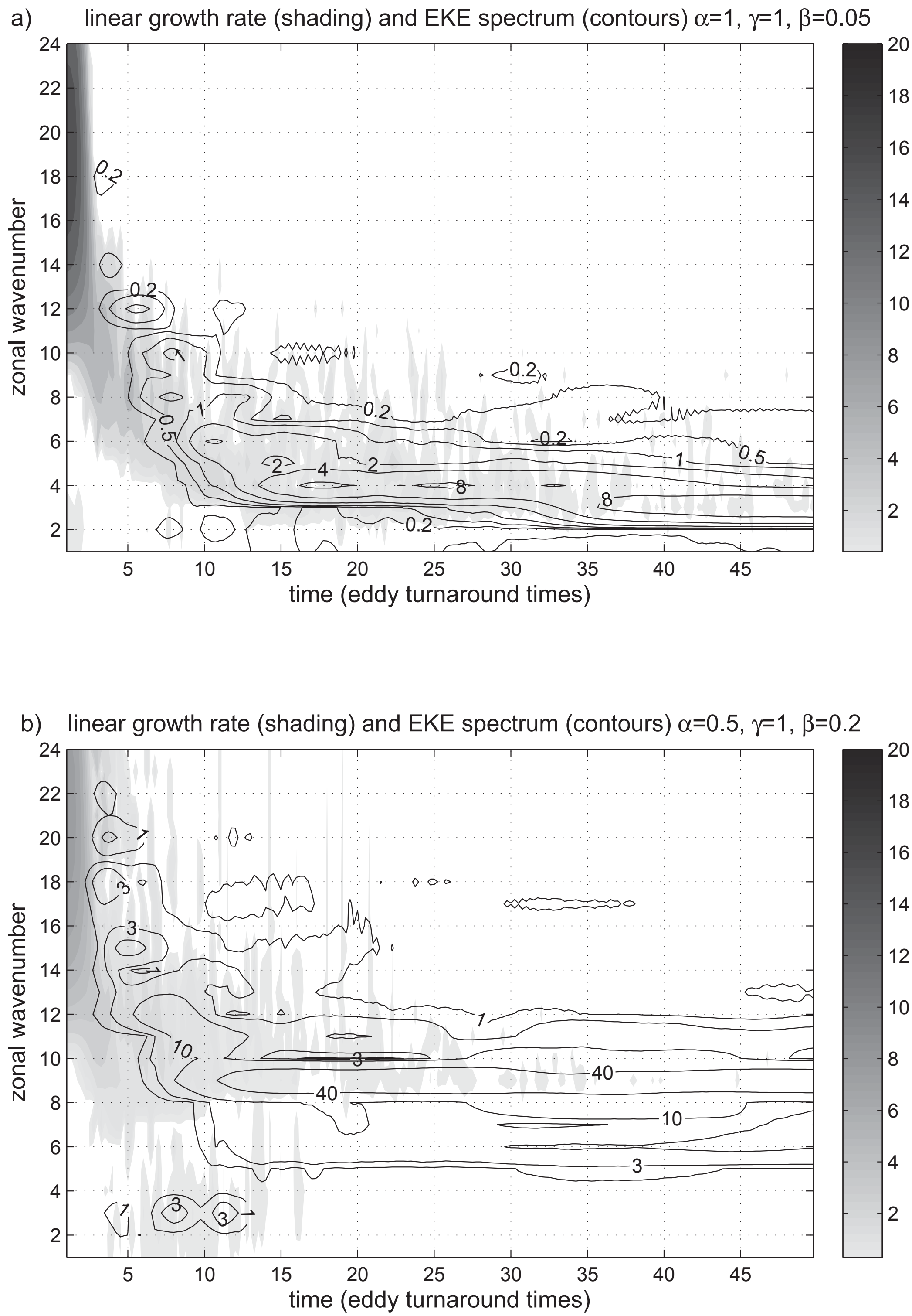

Figure 8: EKE spectrum (contours) and the linear growth rate for the mean flow at each time step (shading): a) for the control run. b) for a run with $\alpha = 0.5$, $\gamma = 1.0$ and $\hat{\beta} = 0.2$.

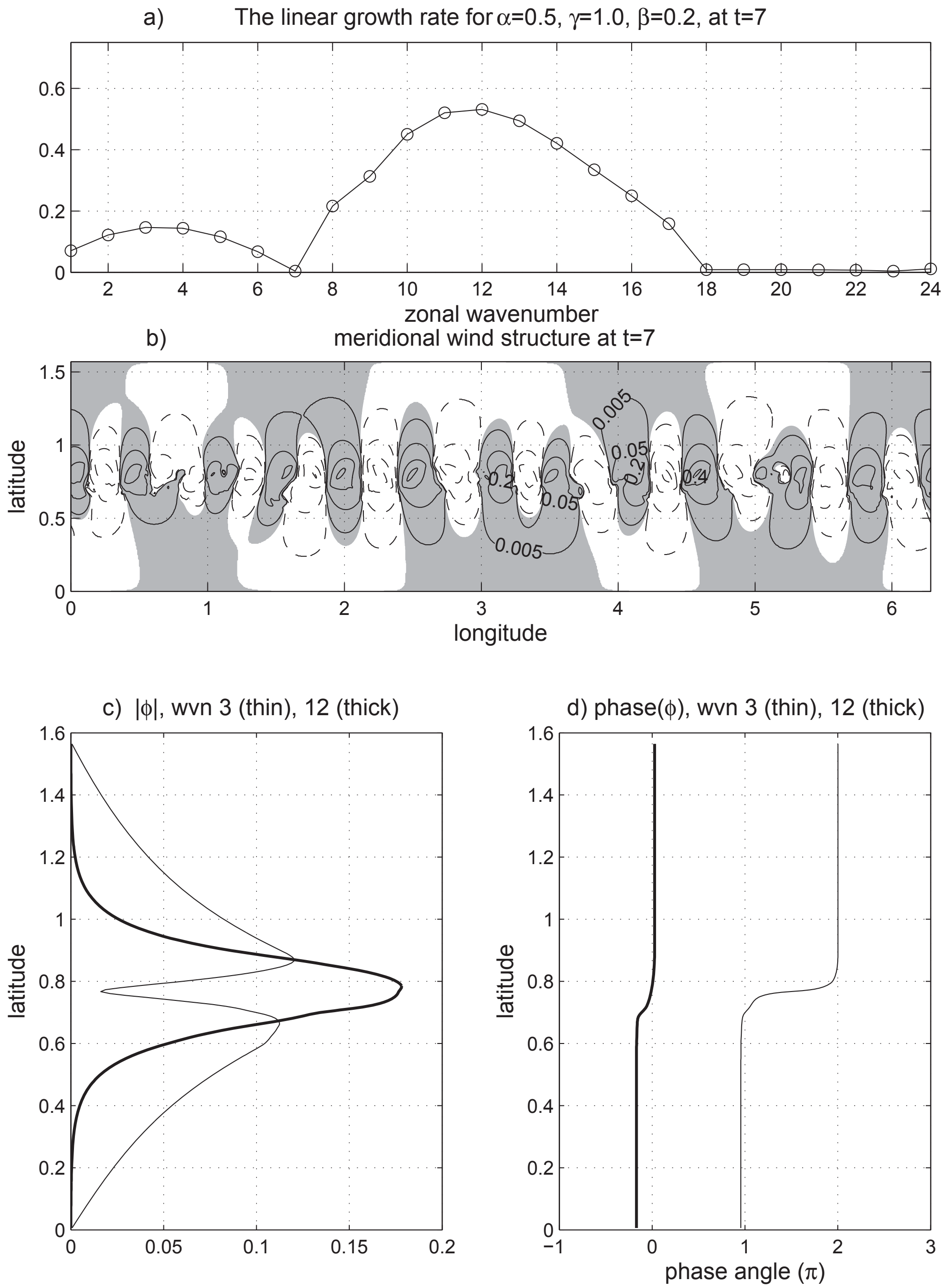

Figure 9: Characteristics of the run with $\alpha = 0.5$, $\gamma = 1.0$ and $\hat{\beta} = 0.2$ (shown in figure 8b) at time $t = 7$: a) the linear growth rate; b) a latitude-longitude section of the meridional wind from the fully nonlinear model run (negative values dashed, positive regions shaded); c-d) the linear geopotential height wave amplitude and phase (units of π), respectively, for zonal wavenumbers $k = 3$ (thin) and $k = 12$ (thick).

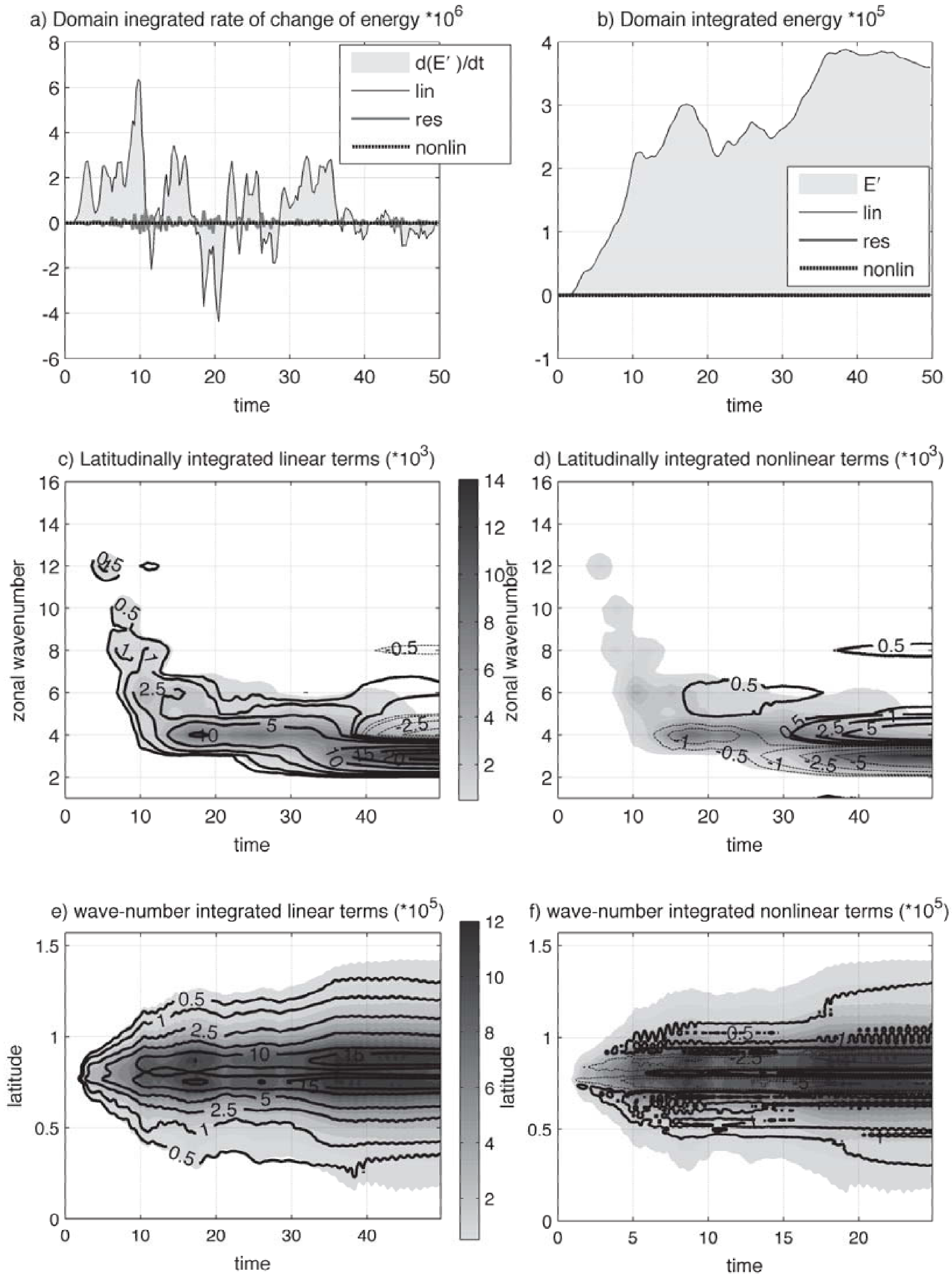

Figure 10: EKE budget for the control run: a) the domain-integrated rate of change of EKE (shading), the contributions of the linear (solid) and nonlinear (dashed) terms, and the residual (EKE growth minus the linear and nonlinear contributions, gray contour); b) The time integral of the quantities shown in a; c) a wavenumber-time plot of the latitudinally-integrated contribution of the linear term to E_k (contours, negative dashed) and the EKE spectrum (shaded); d) as in c but for the nonlinear term; e) latitude-time plot of the spectrally-integrated contribution of the linear term to EKE (contours and shading as in c; f) as in e but for the nonlinear terms.

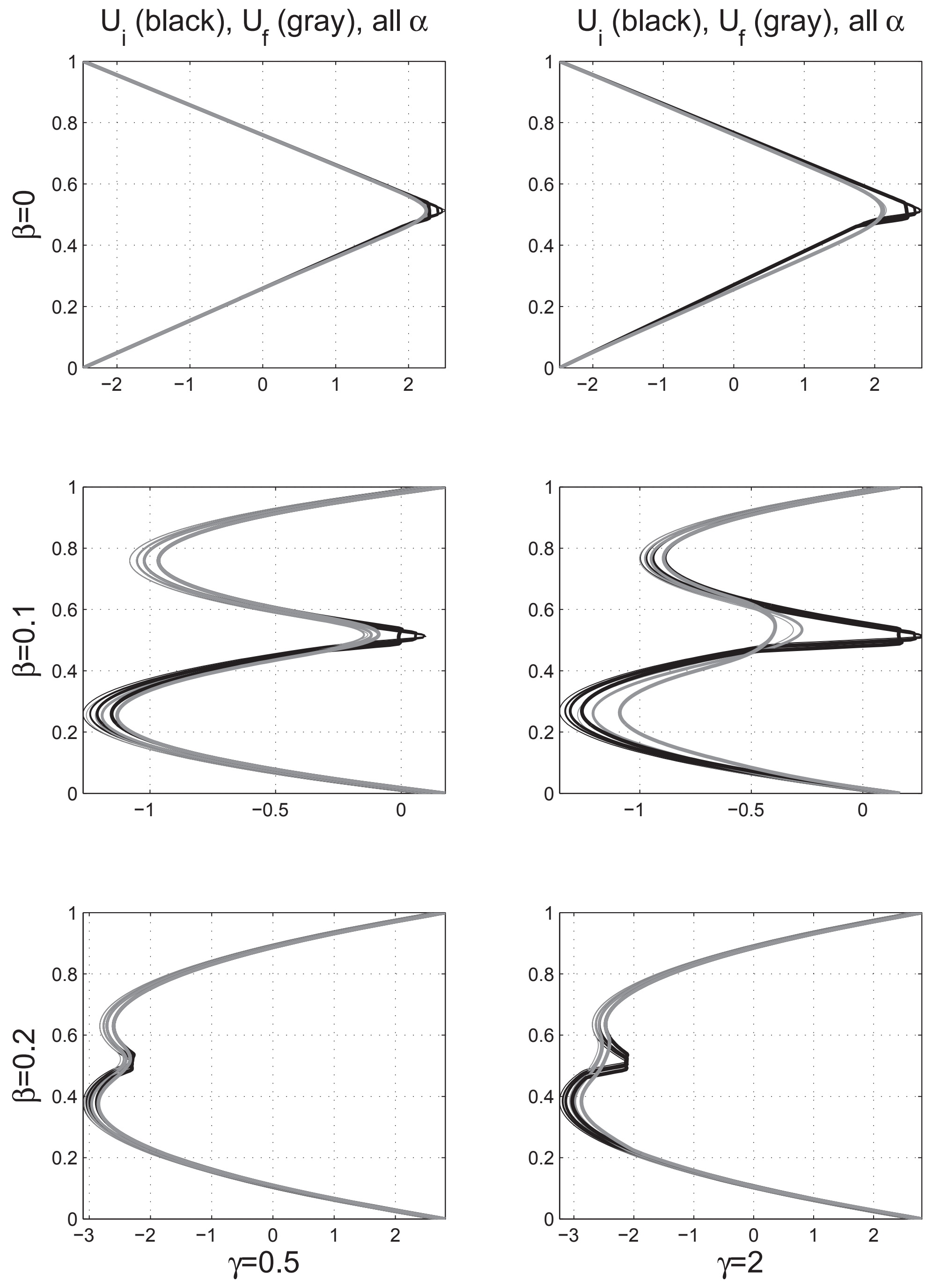

Figure 11: The initial (black) and final (gray) zonal mean zonal wind profiles for a subset of runs in the parameter sweep. The columns, from left to right correspond to $\gamma = 0.5$, 2 respectively, while the rows, from top to bottom, represent $\hat{\beta} = 0$, 0.1, 2, respectively. The line thicknesses correspond to different α values, with the thinnest line representing $\alpha = 0$. Note that for most of the runs, the sensitivity to α (difference in each plot between curves with different thickness) is noticeable only near the jet center.

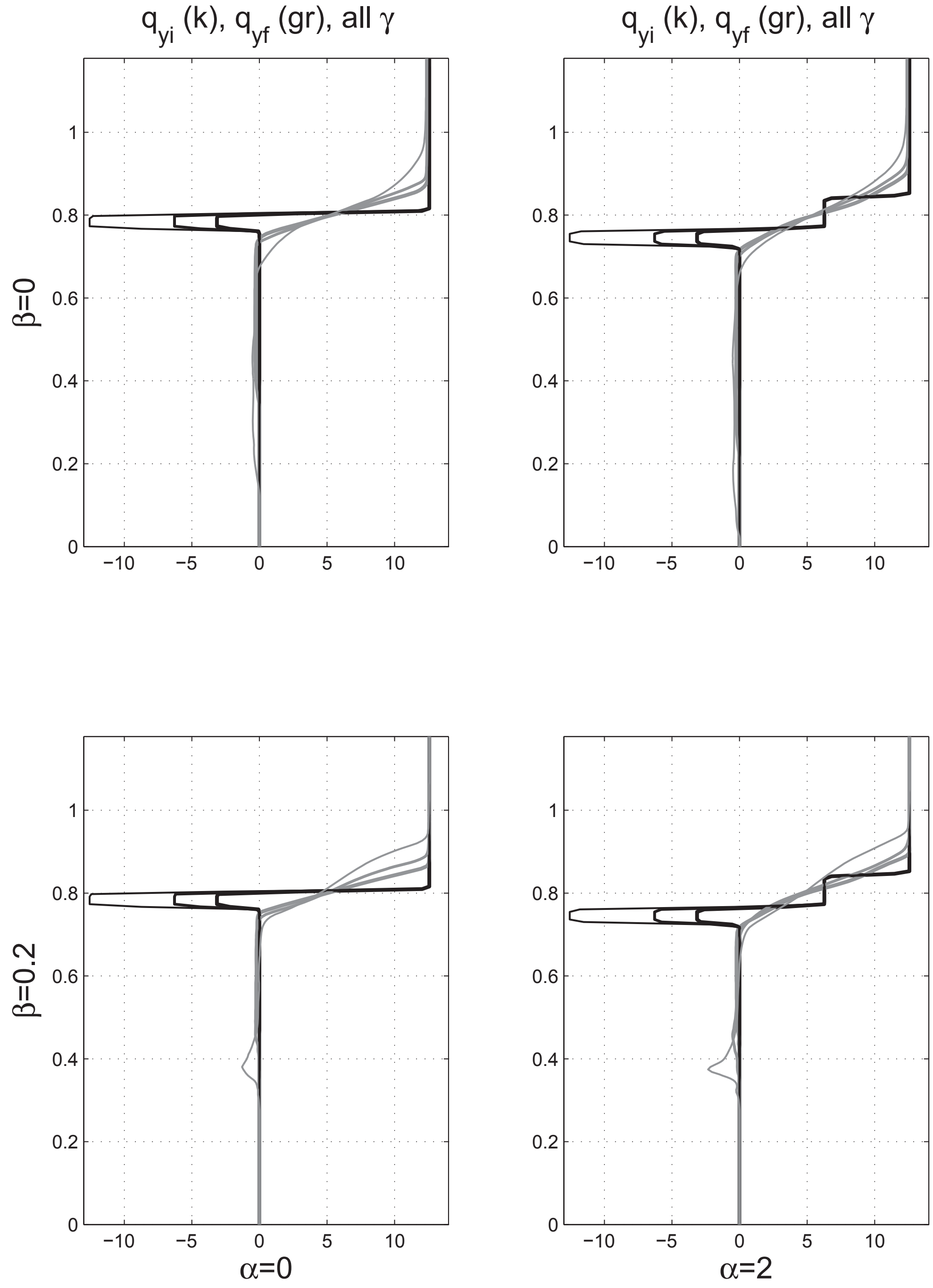

Figure 12: The initial (black) and final (gray) zonal mean PV profiles for a subset of the runs in the parameter sweep. The left and right columns correspond to $\alpha = 0$, 0.2 respectively, while the top and bottom tows, represent $\hat{\beta} = 0$, 2, respectively. The line thickness corresponds to different γ values, with the thinnest line representing the largest γ (2). To highlight the central jump region, the plotting range does not cover all of the model domain.

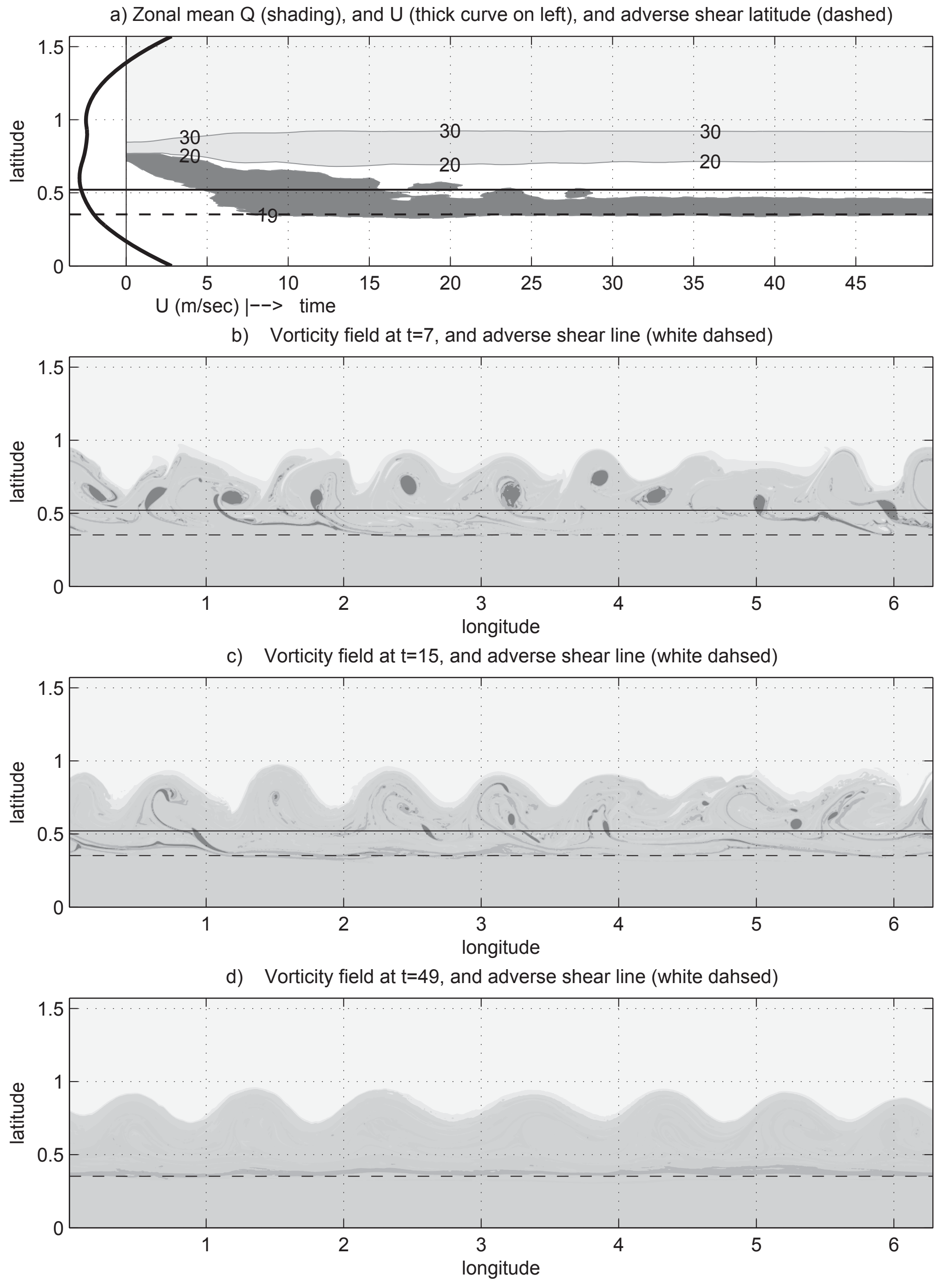

Figure 13: a) Time–latitude plot of the zonal mean PV for the run $\alpha = 2$, $\gamma = 2$, $\hat{\beta} = 0.2$ and the final zonal mean wind profile (thick black curve on left); b-d) instantaneous PV fields for times $t = 7$, 15, 49, respectively, with smaller PV values darker. In all plots, the critical latitudes based on the adverse shear thresholds of 21% (Eq. 10) and 64% (see text for details) are marked by a horizontal black solid and dashed lines respectively.

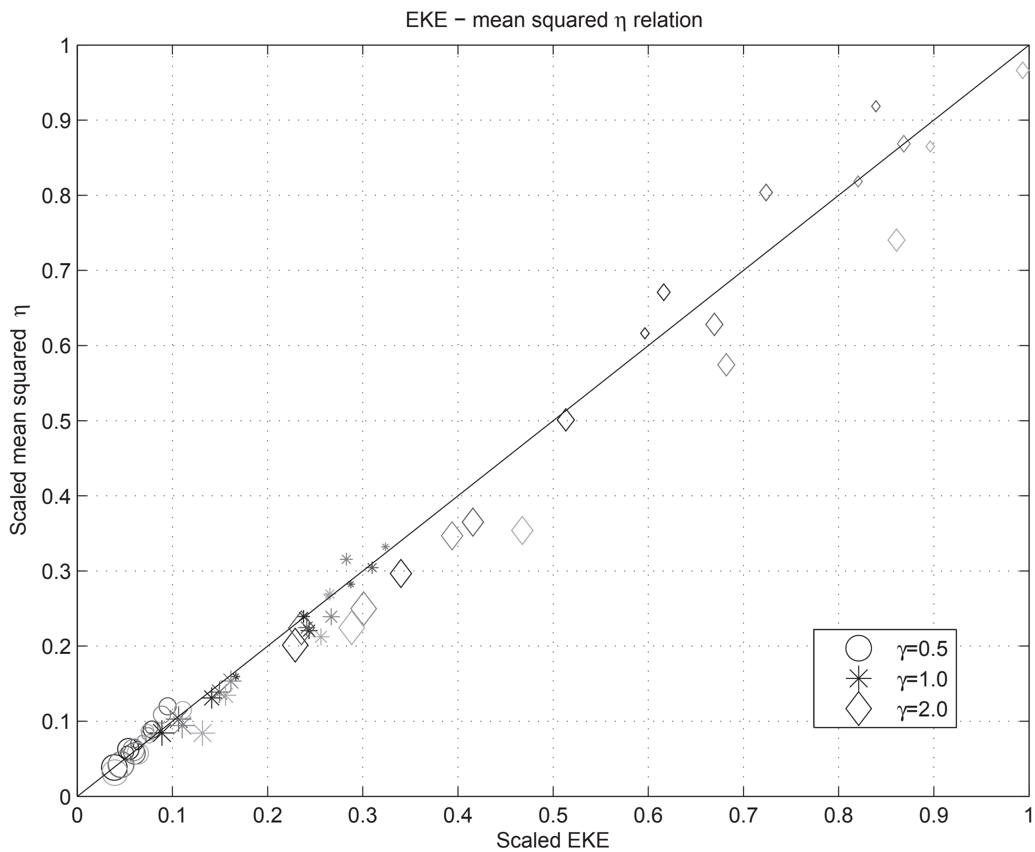

Figure 14: The relation between the equilibrated interface wave amplitude and domain-integrated EKE. Shown are $\overline{\eta^2}/(2k_e(wL_y)^2)$ vs $EKE/(2\pi)^2$. The shape denotes γ, size (from small to large) denotes $\hat{\beta}$, and color (from dark to light) denotes α. The equality line is marked in solid.

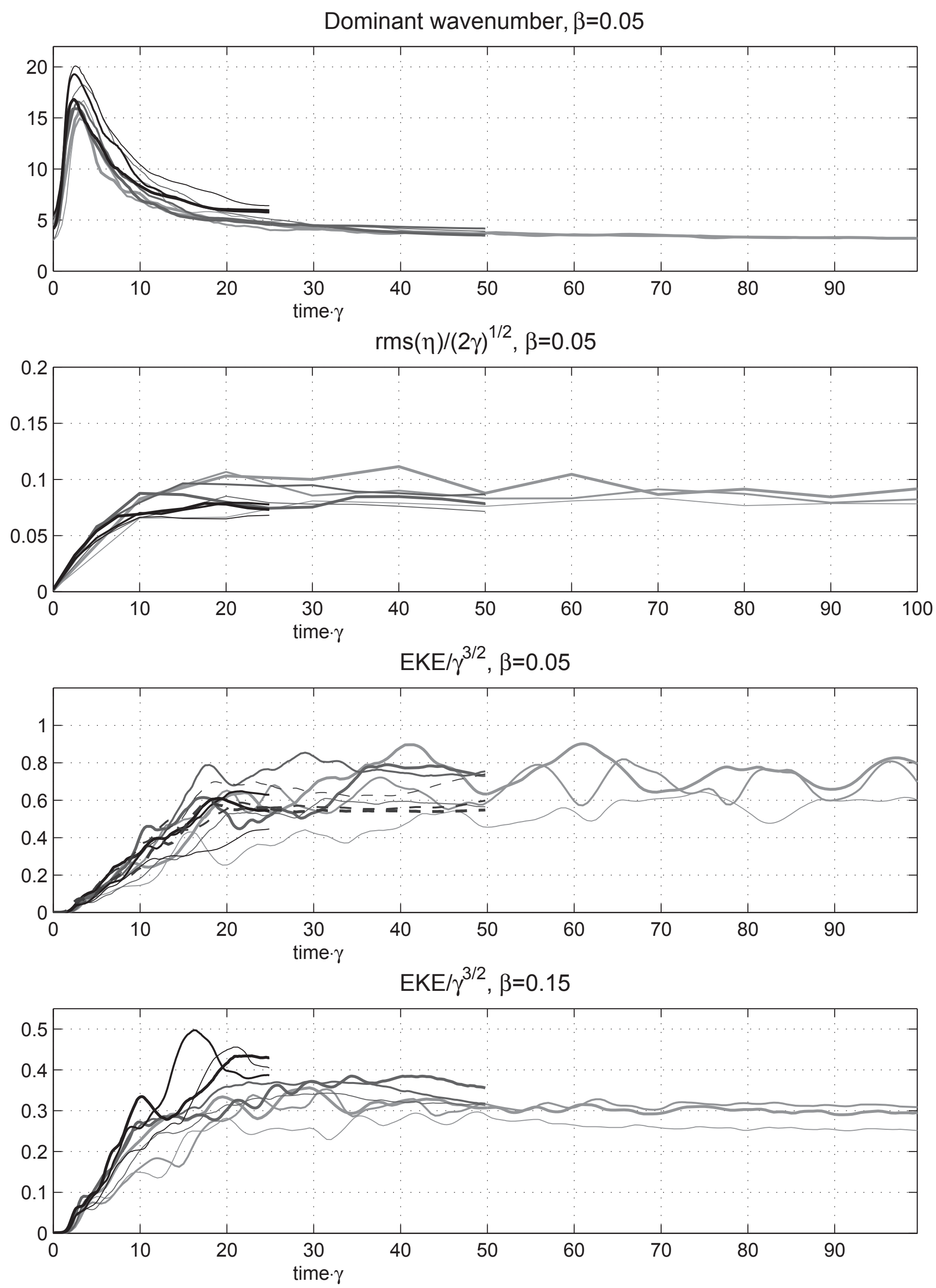

Figure 15: a) k_e as a function of the time scaled by γ, for $\hat{\beta} = 0.05$; b) the rms interface displacement $\overline{\eta^2}^{1/2}$, divided by $2(\gamma)^{1/2}$ for $\hat{\beta} = 0.05$ (note that $\overline{\eta^2}^{1/2}$ was calculated only every 5 time units); c) $\|\mathrm{EKE}\|$ divided by $\gamma^{3/2}$ for $\hat{\beta} = 0.05$; d) As in c) but for $\hat{\beta} = 0.15$. In all plots line thickness denotes α (thinner for smaller α), line colour denotes γ (darker for smaller γ). Note that the length of the time series is proportional to γ. Dashed lines in c) and d) are for longer integrations of the $\gamma = 0.5$ runs needed for full equilibration, and plotted using the same thickness and color coding.

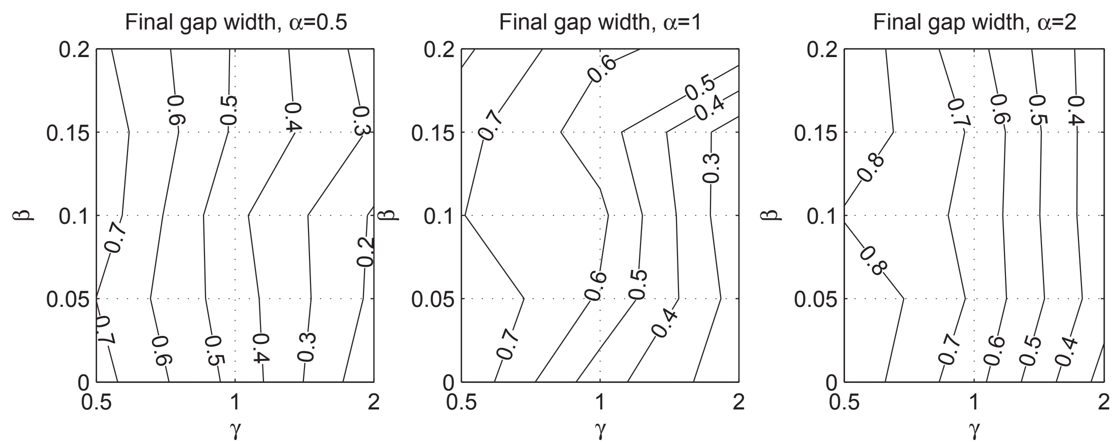

Figure 16: The final relative gap width (with respect to the initial gap width α) as a function of γ and $\hat{\beta}$, for the three non-zero α values.

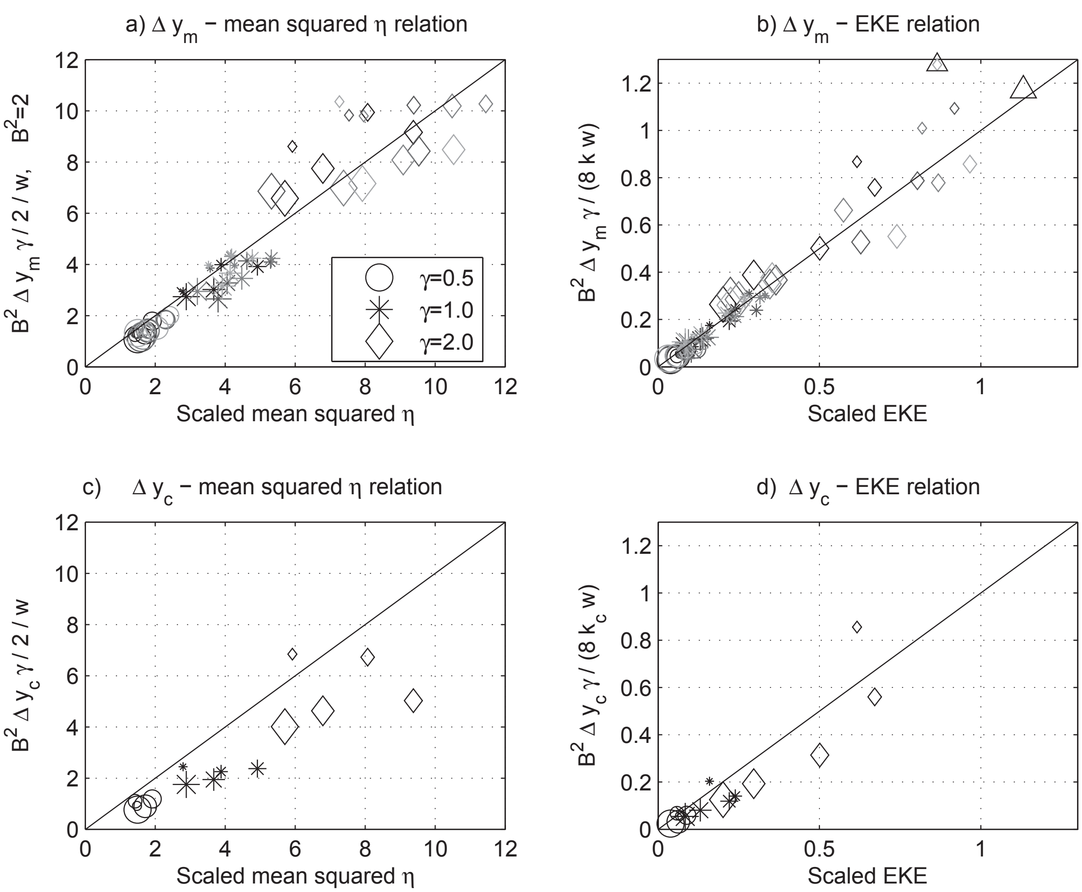

Figure 17: idealized relations between the equilibrated waves and the width of the mixing region. EKE is scaled by $\frac{\pi}{2}(2\pi w)^2$ while $\overline{\eta^2}$ is scaled by $2w^2$

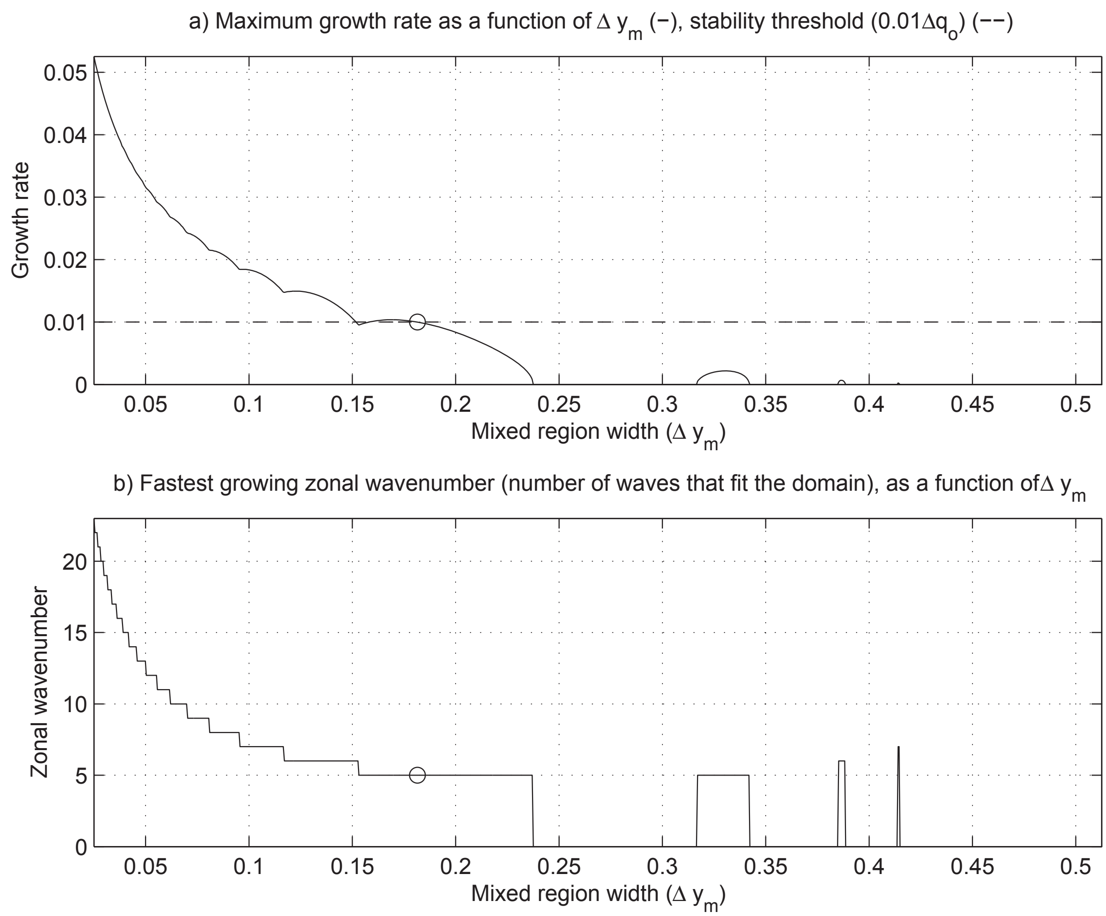

Figure 18: a) The maximum growth rate (scaled by Δq_0) and b) the most unstable zonal wave (number of waves which fit the zonal domain), as a function of the mixed region width (scaled by $L_y = \frac{\pi}{2}$). The dashed line in (a) marks our chosen stability threshold ($0.01\Delta q_0$). The circles mark the marginally unstable case (the largest Δy_m for which the growth rate equals the threshold value).